Aerosol radiative impact during the summer 2019 heatwave produced partly by an inter-continental Saharan dust outbreak. Part 1. Shortwave dust direct radiative effect

Carmen Córdoba-Jabonero[1], Michaël Sicard[2,3], María-Ángeles López-Cayuela[1], Albert Ansmann[4], Adolfo Comerón[2], María-Paz Zorzano[5,6], Alejandro Rodríguez-Gómez[2], Constantino Muñoz-Porcar[2]

[1]Instituto Nacional de Técnica Aeroespacial (INTA), Atmospheric Research and Instrumentation Branch, Torrejón de Ardoz, 28850-Madrid, Spain

[2]CommSensLab, Dept. of Signal Theory and Communications, Universitat Politècnica de Catalunya (UPC), 08034-Barcelona, Spain

[3]Ciències i Tecnologies de l'Espai-Centre de Recerca de l'Aeronàutica i de l'Espai/Institut d'Estudis Espacials de Catalunya (CTE-CRAE/IEEC), Universitat Politècnica de Catalunya (UPC), 08034-Barcelona, Spain

[4]Leibniz Institute for Tropospheric Research (TROPOS), 04318-Leipzig, Germany

[5]Centro de Astrobiología (CSIC-INTA), Ctra. Ajalvir, km. 4, Torrejón de Ardoz, 28850-Madrid, Spain

[6]School of Geosciences, University of Aberdeen, Aberdeen, AB24 3FX, UK

Correspondence to: Carmen Córdoba-Jabonero (cordobajc@inta.es)

Abstract. The shortwave (SW) direct radiative effect during the summer 2019 heatwave produced partly by a moderate, long-lasting Saharan dust outbreak over Europe is analysed in this study. Two European sites (periods) are considered: Barcelona, Spain, (23-30 June) and Leipzig, Germany (29-30 June), 1350 km apart from each other. Major data are obtained from AERONET and MPLNET observations. Modelling is used to describe the different dust pathways, as observed in both sites. The dust coarse (Dc) and fine (Df) components (with total dust, DD=Dc+Df) are identified in the profiles of the total particle backscatter coefficient using the POLIPHON method in synergy with MPLNET measurements. This information is used to calculate the relative mass loading and the centre-of-mass height, as well as the contribution of each dust mode to the DD direct radiative effect (DRE). Several aspects of the aging of dust are put forward. The mean dust optical depth and its Df/DD ratios are, respectively, 0.153 and 24% in Barcelona and 0.039 and 38% in Leipzig; this Df increase in Leipzig is attributed to a longer dust transport path in comparison to Barcelona. The dust produced a cooling effect on the surface with a mean daily DRE of -9.1 and -2.5 W m^{-2}, respectively, in Barcelona and Leipzig, but the Df/DD DRE ratio is larger for Leipzig (52%) than for Barcelona (37%). Cooling is also observed at the top-of-the-atmosphere (TOA), although less intense than on surface. However, the Df/DD DRE ratio at the TOA is even though higher (45% and 60%, respectively, in Barcelona and Leipzig) than on the surface. Despite the predominance of Dc particles under dusty conditions, the SW radiative impact of Df particles can be comparable to, even higher than, that induced by the Dc ones. In particular, the Df/DD DRE ratio in Barcelona increases by +2.4% (surface) and +2.9% (TOA) day^{-1} along the dusty period. This study is completed by a second paper about the

longwave and net radiative effects. These results are especially relevant for the next ESA EarthCARE mission (planned in 2022), as devoted to aerosol-cloud-radiation interaction research.

1 Introduction

Climate change is an important issue nowadays (IPCC, 2013), being extreme events (as heatwaves, droughts, intense aerosol outbreaks, etc.) linked to high perturbations in the radiative balance of the atmosphere. In particular, the knowledge of the aerosol-induced climatological implications is still preliminary, and the uncertainties associated to the determination of the aerosol direct and indirect radiative effects are difficult to be unambiguously estimated. This is mainly due to the change of the aerosol properties during their transport, the incomplete characterization of aerosol complex mixtures and the lack of information on aerosol-cloud interaction mechanisms (i.e., Haywood and Boucher, 2000).

Dust particles play an important role in the frame of climate forcing due to their direct effect on scattering and absorption of solar radiation as well as their indirect effect by acting as both cloud condensation nuclei and ice nucleating particles (deMott et al., 2003). Radiative forcing (RF) is a proxy for climate research and policy, also linked to the change in global mean surface temperature as derived from climate models at continental, regional or local scales. In particular, significant uncertainties in the estimation of the dust-induced direct radiative effects are still present, hence the necessity to study the radiative properties of dust particles, and to adequately quantify their direct effect on the Earth-Atmosphere radiative budget (IPCC, 2013). The direct radiative effect of the total dust has been widely investigated at both shortwave (SW) and longwave (LW) spectral ranges (Sokolik and Toon, 1996; Pérez et al., 2006; Balkanski et al., 2007); however, despite dust intrusions are usually dominated by large particles, the dust fine mode cannot be disregarded, and hence its relative contribution to the total radiative effect. Therefore, the individual radiative estimate for both dust coarse and fine modes must be separately evaluated, and only a few works have addressed this issue. For instance, Sicard et al. (2014b) reported that dust coarse particles seem mainly to affect the LW radiation, being their fine mode mostly responsible of the SW radiative modulation.

Mineral dust is the most abundant aerosol in the atmosphere; however, dust emissions are very difficult to predict. Despite emissions of 1000-3000 Tg yr^{-1} were estimated by global models (i.e., Zender et al., 2004), a later study carried out by means of a global dust model intercomparison (Huneeus et al., 2011) suggested that the emissions may range from 500 to 4000 Tg yr^{-1}. Globally the natural dust sources account for 75%, with the remaining 25% coming from anthropogenic (mainly from agricultural activities) origin (Ginoux et al., 2012). In particular, Saharan dust could represent half of the airborne abundance (Prospero 2002). According to Huneeus et al. (2011), North Africa deserts could emit between 400 to 2200 Tg yr^{-1} of dust particles, hence an 8% of that amount can be attributed to anthropogenic sources (Ginoux et al., 2012). In addition, Saharan dust is frequently transported far from its sources to Europe and the American continent, being able to reach rather high altitudes (up to 8 km height). Hence, changes in the dust properties are expected, influencing their vertical radiative field. Indeed, there is special interest in characterizing the impact of the dust intrusions in the climate of Europe. The arrival of Saharan dust intrusions over Europe is frequently observed in springtime and summertime, mostly in southern Europe; only in very few cases those intrusions are able to reach central and northern Europe (Ansmann et al., 2003; Osborne et al., 2019; Akritidis et al., 2020). Several studies have focused on the dust vertical distribution using ground-based lidar systems (e.g., Ansmann et al., 2003; Papayannis et al., 2005, 2008; Mona et al., 2006; Córdoba-Jabonero et al., 2011), belonging to different aerosol lidar networks (EARLINET, MPLNET). Recent studies have demonstrated that there is an increasing frequency of Saharan outbreaks, in particular, over the Iberian Peninsula (IP) when compared with long-term records (Sousa et al., 2019), with a significant effect on the production of extreme heatwaves over the IP. For instance, the heatwave that occurred in June

2019 over Europe, as described by Sousa et al. (2019), was partly produced by an inter-continental Saharan dust intrusion reaching the IP and central Europe. This dust event is examined in this work.

The aim of this work is threefold: 1) to assess the continuous evolution of the SW direct radiative effect (DRE) of both dust coarse (Dc) and fine (Df) particles during the summer 2019 heatwave over Europe, examining a case study associated to the dust intrusion reaching two European stations in June 2019 by tracking the pathways of the different air masses; 2) to evaluate the impact of the Df particles to the total (Dc+Df) SW DRE; and 3) to show the improved use of polarized Micro-Pulse Lidar (P-MPL) systems, belonging to NASA/MPLNET (Micro Pulse Lidar NETwork, mplnet.gsfc.nasa.gov), for the continuous monitoring of the change of dust properties during transportation, and hence, the DRE evolution. The dust plume was firstly observed in Barcelona (BCN, Spain; 41.4ºN, 2.1ºE, 125 m a.s.l.) on 23 June, and arrived later at Leipzig (LPZ, Germany; 51.4ºN, 12.4ºE, 125 m a.s.l.) on 29 June. Measurements with P-MPL systems were performed in both stations.

The paper is structured as follows: Section 2 describes the instrumentation and methods used, that is: (2.1) the two P-MPL systems as deployed at each of those two urban stations for continuous vertical aerosol observations; (2.2) the retrieval methods to derive the dust properties for both the coarse and fine modes and their vertical mass concentration; (2.3) the radiative transfer (RT) model for DRE calculations; and (2.4) both trajectory and forecast models to simulate the origin and pathways of the dusty air masses; Section 3 describes the results, as obtained on: (3.1) the dust plume origin and transport; (3.2) the separation of dust coarse and fine mode properties; and (3.3) the dust direct radiative effect; and Sections 4 and 5 present, respectively, the discussion of those results and the main conclusions. In a second work (Sicard et al., 2021) the dust longwave and net DRE of the same event are analysed.

2 Materials and Methods

2.1 P-MPL systems

Two polarized Micro-Pulse lidar (P-MPL) systems, belonging to NASA/MPLNET (Micro Pulse Lidar NETwork, mplnet.gsfc.nasa.gov), and deployed at two European urban stations Barcelona (BCN, Spain; 41.4ºN, 2.1ºE, 125 m a.s.l.; permanent location) and Leipzig (LPZ, Germany; 51.4ºN, 12.4ºE, 125 m a.s.l.; planned campaign), were used for vertical dust observations during the dust event examined in this study. BCN and LPZ are located at around 1500 and 2800 km, respectively, from the Saharan dust sources, and at 1350 km apart from each other. Aerosol/cloud profiles are usually recorded in an automatic and continuous (24/7) mode. The P-MPL system is an elastic lidar with a relatively high pulse repetition frequency (2500 Hz) using a low-energy (~ 7 μJ per pulse) Nd:YVO_4 laser at 532 nm, including polarization capabilities. The lidar backscatter signal is registered in the two polarized detection co- (P_{co}) and cross- (P_{cross}) channels, using a unique avalanche photo-detector (APD), sampled for 75-(BCN)/15-(LPZ) m vertical resolution and recorded and integrated for 1-min periods. The total range-corrected signal (RCS) P (Campbell et al., 2002) is the sum of their parallel ($P_p = P_{co} + P_{cross}$) and perpendicular ($P_s = P_{cross}$) signal components, as adapted from Flynn et al. (2007), i.e., $P = P_p + P_s$. Those RCS profiles are averaged for one hour to increase the signal-to-noise ratio. The volume linear depolarization ratio (VLDR), δ^V, can be also estimated from the perpendicular-to-parallel RCS ratio, i.e., $\delta^V = \frac{P_s}{P_p}$. More details of the P-MPL signal processing are described in Córdoba-Jabonero et al. (2018).

2.2 POLIPHON retrieval: separation of the optical and mass features

The POLIPHON (Polarization Lidar Photometer Networking) approach (Mamouri and Ansmann, 2014, 2017) is used in combination with the P-MPL observations (P profiles) for the separation of both fine and coarse extinction components of the desert dust (DD) particles, as described in Córdoba-Jabonero et al. (2018). The algorithm is based on a two-step method for

separating the three components of dusty mixtures. First, by using both the lidar-derived total particle backscatter coefficient (PBC), β_p, and the particle linear depolarization ratio (PLDR), δ_p, profiles, the coarse mode (predominantly, dust coarse particles, Dc), β_{Dc}, and the fine mode of the PBC are separated. Second, the fine mode of the PBC, which is composed of the dust fine particles (Df) and non-dust aerosols (ND), is separated in two more components, respectively β_{Df} and β_{ND}. The ND component is assumed to belong to the fine mode, associated to background (continental, pollution) aerosols in both the urban stations, BCN and LPZ, studied in this work. In summary, the height-resolved total PBC is $\beta_p(z) = \beta_{Dc}(z) + \beta_{Df}(z) + \beta_{ND}(z)$, with z denoting the dependence with height. Particle extinction coefficient (PEC) profiles for each component are obtained from the corresponding PBC and the particular Lidar Ratio (LR, extinction-to-backscatter coefficient ratio) values, S_a, as assumed specific for those Dc, Df and ND components, that is,

$$\sigma_i(z) = S_a^i \, \beta_i(z), \quad (1)$$

where $\sigma_i(z)$, $\beta_i(z)$ and S_a^i are, respectively, the extinction coefficient and the backscatter coefficient as a function of height, and the particular LR for each i component (i.e., i = Dc, Df and ND). In this procedure, specific δ_p and S_a values for each pure Dc, Df and ND components are input parameters. **Table 1** shows the assumed values (corresponding references are also cited).

Total PBC profiles are derived by using the Klett-Fernald (KF) retrieval (Fernald, 1984; Klett, 1985) on the P-MPL RCS measurements and constrained with the Aerosol Optical Depth (AOD) values available from NASA/AERONET network (AErosol RObotic NETwork, aeronet.gsfc.nasa.gov). Columnar AOD data are provided by the two AERONET Cimel sun-photometers, co-located with the P-MPL systems at BCN and LPZ stations. AERONET V3 L2.0 and V3 L1.5 data are available, respectively, from BCN and LPZ sites (see **Sect. 3.3.1**). PLDR profiles are calculated from the PBC and VLDR profiles. More details of the P-MPL signal processing and optical retrieval are described in Córdoba-Jabonero et al. (2018). Relative uncertainty values associated to those optical properties are shown in **Table 2**.

Additionally, once σ_{Dc}, σ_{Df} and σ_{ND} are determined, the mass concentration (MC) profiles of each i component, $m_i(z)$ (g m^{-3}; i = Dc, Df and ND), can be calculated (the expected values with relative uncertainties are included in **Table 2**) with the relation (Ansmann et al., 2017; Córdoba-Jabonero et al., 2016, 2019)

$$m_i(z) = f_m^i \, \sigma_i(z), \quad (2)$$

where f_m^i (g m^{-2}) are the specific AERONET-based extinction-to-mass conversion factors (Ansmann et al., 2019) for each component (i = Dc, Df and ND). Note that

$$f_m = d_p \, c_v = k_m^{-1}, \quad (3)$$

where d_p, c_v and k_m are, respectively, the particle density (g cm^{-3}), the volume conversion factor (10^{-12} Mm) and the mass extinction efficiency (MEE, m^2 g^{-1}). The assumed values of all those parameters are shown in **Table 1**. The vertical profile of the total mass concentration, M_C (g m^{-3}) is calculated as the summatory of each mass component, i.e.,

$$M_C(z) = \sum_i m_i(z), \quad (4)$$

and their vertically-integrated mass values (i.e., mass loadings, g m^{-2}), denoted as ml_i and M_L, are

$$ml_i = \sum_z m_i(z) \, \Delta z, \text{ and} \quad (5)$$

$$M_L = \sum_z M_C(z) \, \Delta z, \quad (6)$$

where Δz is the vertical resolution of the lidar measurements (75 and 15 m, respectively, for BCN and LPZ).

Table 1: Assumed specific values of PLDR (δ_p) and LR (S_a, sr) together with the mass conversion factor (f_m, g m^{-2}), particle density, d_p (g cm^{-3}), volume conversion factor (c_v, 10^{-12} Mm) and MEE (k_m, m^2 g^{-1}) for the Dc, Df and ND components.

Parameter	Dc	Df	ND	References
δ_p	0.39	0.16	0.05	Mamouri and Ansmann (2017)
S_a	55	55	50	Ansmann et al. (2017)
c_v	0.83 (*)	0.23 (*)	0.30 (**)	(*) Ansmann et al. (2019), for the North African region (**) Mamouri and Ansmann, (2017)
d_p	2.6	2.6	1.55	Mamouri and Ansmann, (2017)
f_m	2.16	0.60	0.465	**Eq. 3** (this work)
k_m	0.46	1.67	2.15	**Eq. 3** (this work)

The relative height-integrated mass contribution of each component with respect to the total mass loading, M_i (%) (i = Dc, Df, and ND), which is expressed as

$$M_i = \frac{ml_i}{M_L} \times 100, \quad (7)$$

is also examined during the dust event as observed in BCN and LPZ.

Regarding the vertical impact of each component, their relative contribution in terms of a mass-weighted altitude, the so-called center-of mass (CoM) height, is calculated, and its evolution is examined along each particular dust event period in BCN and LPZ. The CoM height, Z_m, is defined similarly as in Córdoba-Jabonero et al. (2019), that is,

$$Z_m^i = \frac{\sum_k z_k\, m_i(z_k)\, \Delta z}{\sum_k m_i(z_k)\, \Delta z}, \quad (8)$$

being $m_i(z_k)$ the mass concentration profile for each i component (see **Eq. 2**, with i = Dc, Df and ND), and z_k the height, where k denotes the height-step defined by the vertical resolution, Δz (75 and 15 m, respectively, for BCN and LPZ measurements).

Table 2. Relative uncertainties (%) associated to the lidar-derived particle optical properties and mass features (i is for the Dc, Df and ND components).

Parameter		Dc	Df	ND
β_p	10 - 15			
δ_p	15 - 25			
σ_i		25 – 30	40 – 50	25 - 30
m_i		25 – 30	40 – 50	35 - 40

2.3 GAME radiative transfer model

Solar flux was calculated for 18 layers of the atmosphere distributed between the ground level and 20-km height with the radiative transfer (RT) model GAME (Dubuisson et al., 1996; 2004; 2006). The solar spectral range was set from 0.2 to 4.0 μm (wave number resolution of 400 cm^{-1} from 0.2 to 0.7 μm and 100 cm^{-1} from 0.7 to 4.0 μm). GAME calculates solar flux values at the boundary of plane and homogenous atmospheric layers by using the discrete ordinates method (Stamnes et al., 1988). Gas (H_2O, CO_2, O_3, N_2O, CO, CH_4 and N_2 are considered) absorption is calculated from the correlated k distribution (Lacis and Oinas, 1991). More details about the computation of the gas transmission functions can be found in Dubuisson et al. (2004) and Sicard et al. (2014a). The gas absorption is parametrized from profiles of pressure, temperature and relative humidity. In BCN, radiosoundings launched twice a day (at 00 and 12 UT) by the University of Barcelona in collaboration with the Servei Meteorològic de

Catalunya, the Catalonia meteorological agency, were used. No radiosoundings are available in LPZ, thus the 6-hour profiles from the Global Data Assimilation System (GDAS) provided by the National Oceanic and Atmospheric Administration (NOAA) were used instead. Aerosols are fully parametrized in the GAME model by the user in terms of spectrally- and vertically-resolved aerosol optical depth (AOD), single scattering albedo (SSA) and asymmetry factor (asyF). The spectrally-resolved surface albedo (SA) is another input of the model. All those latter parameters are described in **Section 3.3.1**.

GAME has been used to calculate solar flux values for scientific purposes in several works (e.g., Roger et al., 2006; Mallet et al., 2008; Sicard et al., 2012). It was validated by means of an intercomparison exercise of radiative transfer models (Halthore et al., 2005) which concluded that GAME is accurate to a few units of watt (1–3) for an incoming solar flux of 1000 W m^{-2}. Since this work is focused on the dust radiative impact, the expression of the aerosol direct radiative effect (ARE) is particularly defined for dust as the dust direct radiative effect (DRE), at a given height level, L, that is,

$$DRE(L) = \left[F_d^{\downarrow}(L) - F_d^{\uparrow}(L)\right] - \left[F_0^{\downarrow}(L) - F_0^{\uparrow}(L)\right], \quad (9)$$

where F_d and F_0 are the radiative flux values with and without dust, while the ↓ and ↑ arrows indicate whether the fluxes are downward or upward, respectively. By that definition, negative (positive) DRE values represent a cooling (warming) effect. The DRE was calculated at two climate-relevant altitude levels: at the top-of-atmosphere (TOA) and on surface (SRF). The dust contribution in the atmospheric column is quantified by the atmospheric radiative effect, $DRE(ATM)$, which is defined as:

$$DRE(ATM) = DRE(TOA) - DRE(SRF) \quad (10)$$

2.4 Air masses transport modelling

In order to determine the origin and pathway of the dusty air masses affecting both stations involved in this study, a trajectory analysis using two different models is performed. The Hybrid Single Particle Lagrangian Integrated Trajectory (HYSPLIT) model Version 4, developed by NOAA's Air Resources Laboratory (ARL) (https://www.ready.noaa.gov/HYSPLIT.php; Draxler and Hess, 1998; Stein et al., 2015; Rolph et al., 2017) is used in conjunction with the Global Data Analysis System (GDAS) meteorological files (https://www.emc.ncep.noaa.gov/gmb/gdas/; spatial resolution of 1º x 1º every 3 hours) in order to identify the source regions of the dust particles. HYSPLIT 5-day back-trajectories of air masses arriving at each one of both stations (BCN and LPZ) are obtained. The NMMB/BSC-Dust model (https://ess.bsc.es/bsc-dust-daily-forecast; Pérez et al., 2011) is an online multi-scale atmospheric dust model providing short- to medium-range dust forecasts for both regional and global domains. It has been designed and developed by the Barcelona Supercomputing Center (BSC) and is fully embedded into the Non-hydrostatic Multiscale Model (NMMB) developed at NOAA/National Centers for Environmental Prediction (NCEP) (Janjic et al., 2011). This toll has been used to obtain dust forecasts over both BCN and LPZ stations during the period from 23 to 30 June 2019.

3 Results

This section is divided in three subsections on: the dust plume origin and transport, the application of the POLIPHON algorithm to the P-MPL observations in terms of dust coarse and fine mode contributions to the optical and mass products, and the estimation of the dust direct radiative forcing.

3.1 Dust plume origin and transport

The summer 2019 heatwave as observed across Europe (Sousa et al., 2019) was produced partly by an inter-continental Saharan dust outbreak. An overview of this dust intrusion coming from the African continent to Europe, mostly observed from 23 to 30 June 2019, is illustrated with the NMMB/BSC-Dust forecast images. **Figure 1** shows the Dust Optical Depth (DOD) at 550

nm and the 700 hPa wind field (the position of BCN and LPZ stations is marked, respectively, by a red and a blue point). On 24 June 06 UT, DOD values greater than 0.15 were observed at BCN, with stable dust conditions throughout the study period. The Saharan dust outbreak moved towards North Europe and looped down on 29 June, reaching LPZ at 12UT. In this station, unlike in BCN, two consecutive, close in time, dust events occurred. DOD values greater than 0.15 were first observed until the early hours of 30 June (first dust period in LPZ). This was followed by non-dust conditions until 14UT, when dust evidence was detected again until the end of the day (second dust period).

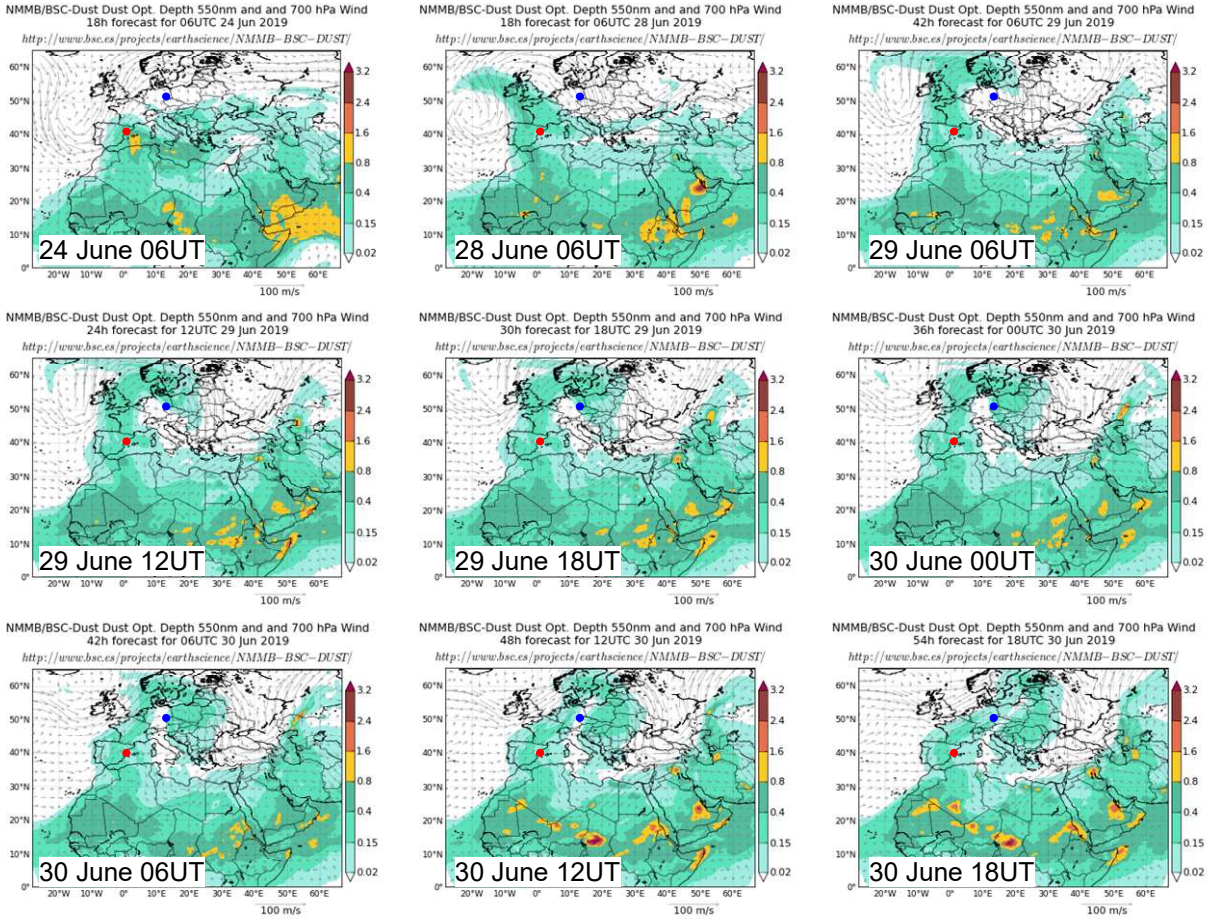

Figure 1: NMMB/BSC-Dust forecast images showing both the Dust Optical Depth at 550 nm and 700 hPa wind field, illustrating the inter-continental Saharan dust outbreak observed from 23 to 30 June 2019. Both stations: BCN (41.4ºN, 2.1ºE) and LPZ (51.4ºN, 12.4ºE) are marked, respectively, by a red and a blue point. Dates and times are indicated in each image).

A similar pattern is found by analyzing the HYSPLIT 5-day height-dependent back-trajectories shown in **Figure 2**. Regarding the particular height-dependent back-trajectories over BCN , Saharan air masses at 2500 and 4000 m coming from North Africa can be observed for the whole dust event (23-30 June) (see **Fig. 2**; note that dates and times are the same as those shown in **Fig. 1**).On the other hand, those observed at 4500 m over LPZ from 29 to 30 June mainly come from the Iberian Peninsula, which was still under dust outbreak conditions in the same period. This indicates that the dusty conditions observed at LPZ are due to dust transport from the Iberian Peninsula (i.e., BCN area), observing two slightly separated dust events. The first one, occurred from 29 June 12UT to 30 June 05UT, reached altitudes higher than 3000 m height, while the second one (from 30 June 15UT to the end of the day) was detected at lower heights (see **Fig. 2**).

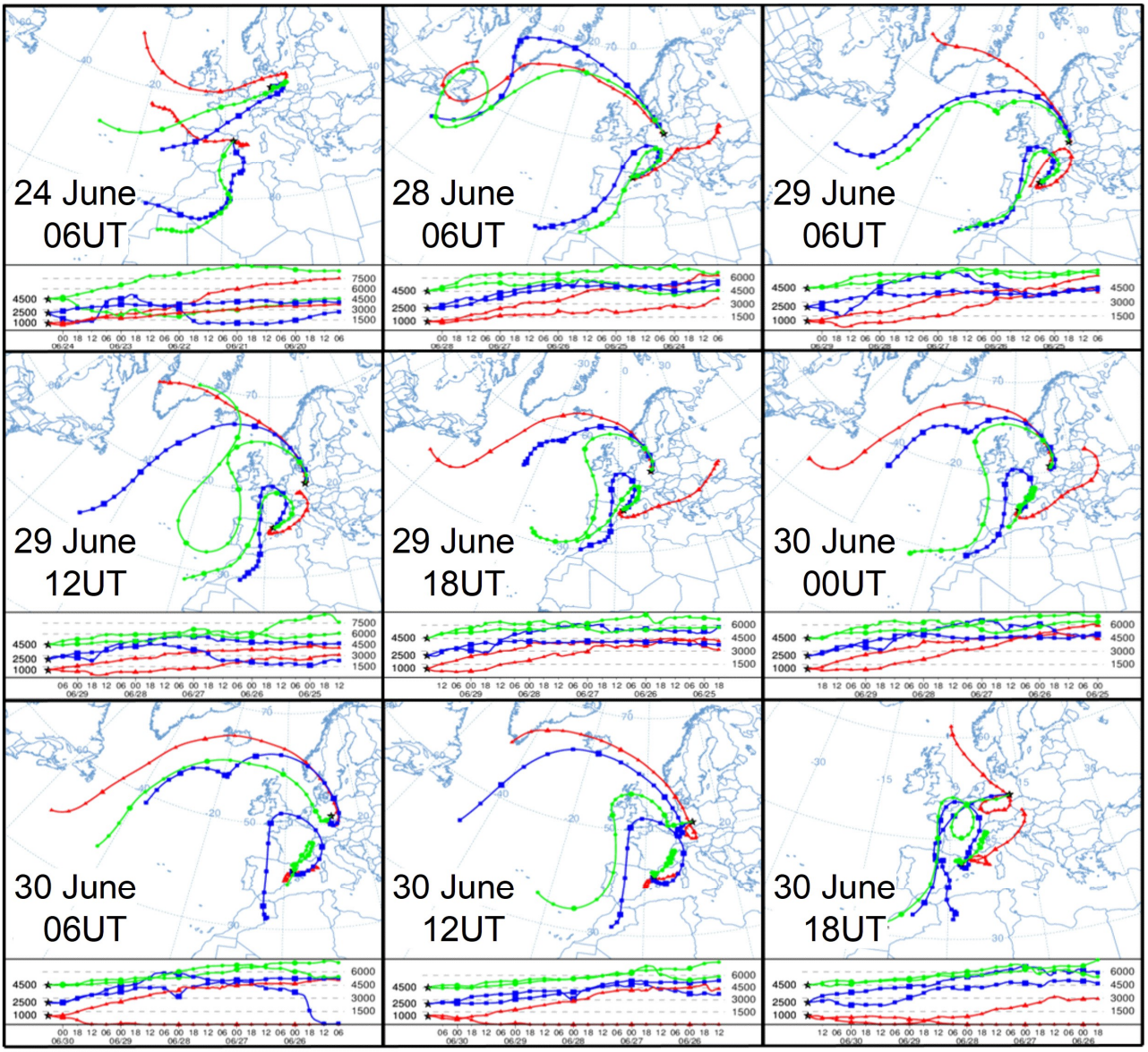

Figure 2: HYSPLIT 5-day back-trajectories arriving at altitudes of 1000 (red), 2500 (blue) and 4500 (green) m a.g.l. over BCN (Spain, 41.4ºN 2.1ºE) and LPZ (Germany, 51.4ºN 12.4ºE) (marked by black stars), illustrating the inter-continental Saharan dust outbreak observed from 23 to 30 June 2019. Note that dates and times are the same as those shown in Fig. 1 (also indicated in each plot).

3.2 Dust coarse/fine mode separation

3.2.1 Optical properties: backscatter coefficient and depolarization ratios

The evolution of the aerosol optical properties during the dusty events as observed at BCN (23-30 June) and LPZ (29-30 June) is analysed regarding their vertical structure. **Figure 3** shows the total PBC, β_p, and those separated into dusty, β_{Dc} and β_{Df}, and non-dusty, β_{ND}, components, together with the PLDR, δ_p, and VLDR, δ^V, for representative cases of that evolution (date and times are shown in each panel, corresponding to the HYSPLIT images shown in **Fig. 2)**.

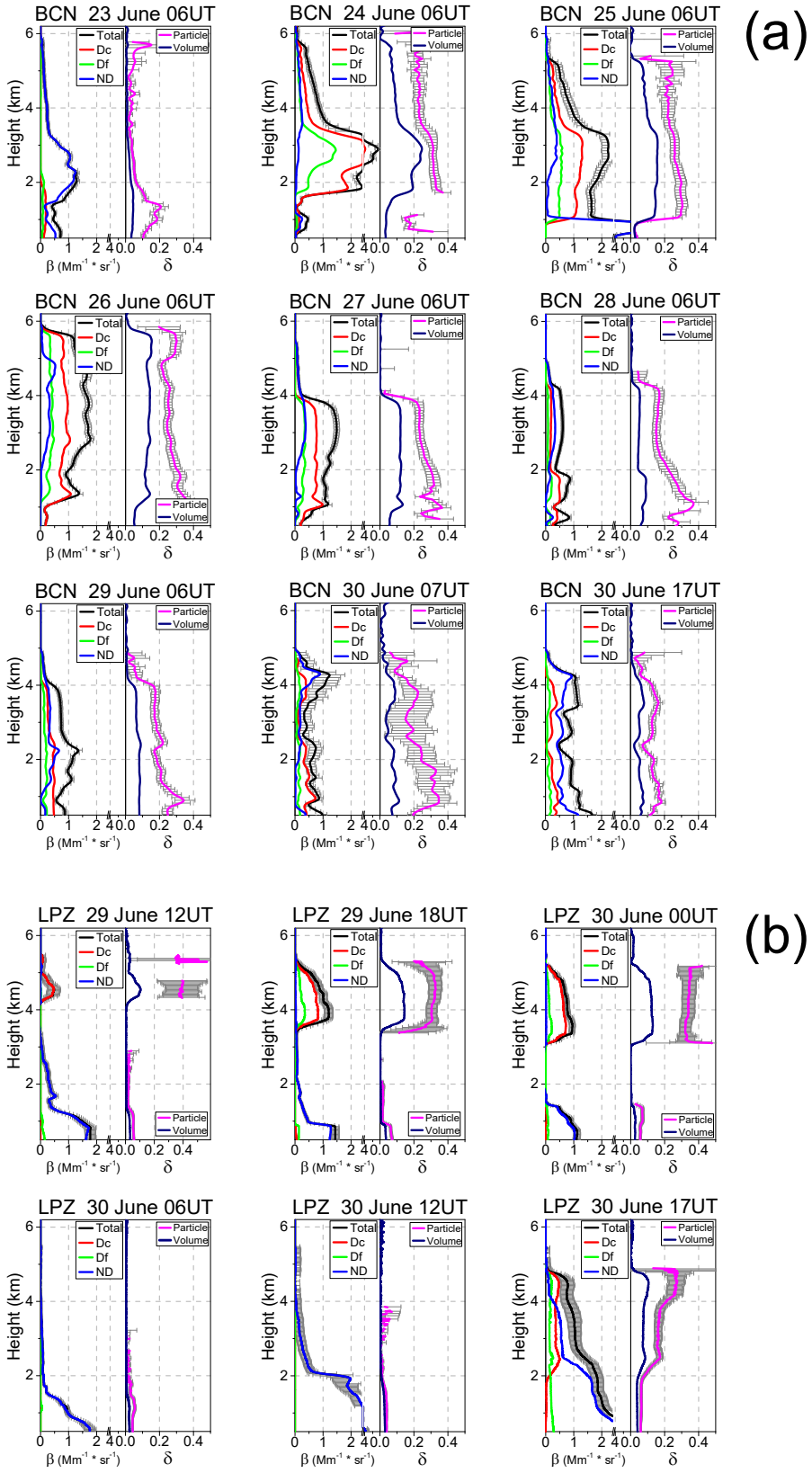

245 **Figure 3: Vertical profiles of the optical properties for representative cases (date and time are shown in each panel) of the dusty events as observed at (a) BCN and (b) LPZ: the total β_p (black), and those separated into dusty (β_{Dc}, red, and β_{Df}, green) and non-dusty (β_{ND}, blue) components (Left panels), together with δ^V (dark blue) and δ_p (magenta) (Right panels). These particular cases**

are marked by black circles in Fig. 4. For clarity, errors (grey bars) are shown only for β_p and δ_p (particular uncertainties are in Table 2).

In general, by looking at the successive selected panels in **Figure 3-a**, a gradual dust occurrence can be observed at BCN during the whole dusty event. The greatest incidence of dust intrusion is observed on 24 June, showing a pronounced dust (DD=Dc+Df, with Dc predominance) layer, extending from 1.5 to 5.5 km height and with a total PBC peak of 5.6 ± 0.4 Mm^{-1} sr^{-1} at around 3 km height.. In this dust layer, the mean δ_p is 0.31 ± 0.02 from 1.5 to 3.5 km, decreasing to 0.23 ± 0.01 at higher altitudes, up to 5.5 km. Also, a narrow dust layer with a mean δ_p of 0.28 ± 0.06 is found above, at around 6.2 km height. During the following days, a DD layer with a small ND contribution, also extensively ranging from 1 km to, respectively, 5 km (25 June) and 6 km (26 June) height can be observed. In this case, the dust incidence is smaller: β_p peak values of 2.2 ± 0.2 and 1.8 ± 0.1 Mm^{-1} sr^{-1} are found on 25 and 26 June (approx., 30-40% of that on 24 June), respectively, with mean δ_p values of 0.25 ± 0.04 and 0.27 ± 0.03. On 27 June, the DD layer descends down (0-4 km), with β_p of 1.5 ± 0.1 Mm^{-1} sr^{-1} and similar δ_p values (0.26 ± 0.05, in average). On 28 and 29 June, the DD signature is also observed from around 4 km down to the surface; however, the main DD occurrence is found from 2.0-2.5 km, with a weaker dust incidence: the β_p peak is less than 1 and around 1.4 Mm^{-1} sr^{-1} on 28 and 29 June, respectively (i.e., around 17 and 25% of that found on 24 June). Regardingδ_p values found on 28 and 29 June, they are smaller than 0.20 (with mean values of 0.15 ± 0.05 and 0.14 ± 0.06, respectively) above 2 km, and 0.28 ± 0.04 and 0.25 ± 0.04, in average, below 2 km. As stated before, this points out that the DD signature is more intense at heights lower than around 2 km. Similarly, the DD incidence still decreases on 30 June, being rather low in the afternoon, with δ_p values smaller than 0.2 (0.12 ± 0.04, in average), indicating the final stage of the dust event over BCN.

In the case of the dust intrusion at LPZ, the dust pattern is different from that observed at BCN site, as also confirmed by BSC/NMMB-Dust and HYSPLIT modelling (see **Figs. 1** and **2**). During the 29-30 June dust event, two dusty periods can be differentiated. The first one starts on 29 June at 12UT, when a two-peak emerging dust layer (4.5 and 5.3 km)with δ_p values close to 0.4, indicating a major presence of Dc particles (Mamouri and Ansmann, 2017) (see **Fig. 3b**, 29 June 12UT), is observed, and finishes on 30 June at 05UT. The second one extends from 30 June at 13UT to the end of that day (unfortunately, no P-MPL data were available after 18UT). **Figure 3b** illustrates the evolution of the dust intrusion once arrived at LPZ on 29 June at 12UT. For the first dusty period, from 18UT on, a well-developed two-layered structure is observed: an evident DD layer with a high predominance of Dc particles is clearly confined from 3.5 to 5.5 km height, and no DD signature at lower altitudes can be detected. In this dust layer, β_p peak values are between 0.9 and 1.2 (± 0.03, in average) Mm^{-1} sr^{-1}, showing a lower dust incidence (16-21%) with respect to BCN, and only comparable with that present during the last days. However, δ_p values are higher, ranging between 0.39 ± 0.07 at the beginning and 0.31-0.34 (± 0.02) later on the episode, indicating a high predominance of Dc particles (Mamouri and Ansmann, 2017). On the second dust period, a mixing of Dc, Df and ND particles is observed (see **Fig. 3b**, 30 June 17UT): the DD layer is extended from the ground to 5 km height, approximately, but with a weak incidence (β_p = 0.3-0.8 Mm^{-1} sr^{-1}). The DD signature below 2 km only corresponds to Df particles, scarcely present in this layer, where the ND aerosols dominate, as indicated by the meanδ_p = 0.063 ± 0.003 in this layer. The Dc and Df components are mainly present in layers at higher altitudes, as also indicated by the PLDR: mean δ_p values of 0.25 ± 0.03 and 0.16 ± 0.03 are found, respectively, in layers ranging from around 4 to 5 km and from 2 to 4 km height, representing a dominant presence of Dc particles in the first of those layers.

3.2.2 Mass features: relative mass loadings and centre-of-mass height

The aerosol mass features during the dusty events as observed at BCN (23-29 June; continuous dust incidence) and LPZ (29J-30 June; two separated dust episodes) are analysed in terms of the relative mass contribution of the Dc, Df and ND components, and their centre-of-mass (CoM) height, as a measure of the vertical mass impact of each component. **Figure 4** shows the time evolution of the relative mass loading for each component, M_i (%) (i: Dc. Df, and ND; see **Eq. 7**) together with the total mass loading, M_L (g m^{-2}, top panels), and the CoM height, Z_m (km, bottom panels), for each component along the particular dust event. Daily- (BCN) and episode- (LPZ) averaged M_L and Z_m values are denoted using a bar over the variable, i.e., $\overline{M_L}$ and $\overline{Z_m}$. A maximal $\overline{M_L}$ of 0.66 ± 0.42 g m^{-2} is found on 24 June at BCN, representing 3-5 times higher than those maxima observed in LPZ (0.14 ± 0.03 and 0.20 ± 0.04 g m^{-2}, respectively, for the first and second episodes). That high dispersion found for $\overline{M_L}$ (~ 64%) is due to the high variability of the dust mass loading along this day, showing a pronounced M_L peak of 1.97 ± 0.6 g m^{-2} at 11UT (88 and 9% of that corresponding to the contribution of the Dc and Df particles, respectively).

In general, as shown in **Figure 4 (top panels)**, Dc particles are mostly dominating over BCN (M_{D_c} > 80%) during the 59% of the overall dust period (23-30 June), though, prevailing for the 90% of that time in a rather high percentage (M_{D_c} around 60%); the Df presence is significantly lower (M_{D_f} < 10% for the 72% of the dust length). Comparable results are found in BCN under dusty conditions, when similar extinction-to-mass conversion factors are provided (Hess et al., 1998; Ansmann et al., 2019), only depending on the strength (intense and extreme) of dust intrusions (Córdoba-Jabonero et al., 2018, 2019). The relative Df mass contribution with respect to the total dust mass loading is 11%. , The mean daily-averaged mass loading is 0.28 ± 0.17, 0.03 ± 0.02 and 0.31 ± 0.19 g m^{-2}, respectively, for Dc, Df and DD components for the whole 23-30 June period (see **Table 4**). As a comparison, during an extreme dust situation over BCN (Córdoba-Jabonero et al., 2019) mass loadings reached up to 2.8 g m^{-2} .

However, the situation at LPZ is slightly different. The relative Dc (Df) contribution during the first dust episode is lower than (similar to) that at BCN (M_{D_c} = 68% and M_{D_f} = 9%, in average). During the second episode, despite the mean $\overline{M_L}$ is 1.50 times higher than in the first one, M_{D_c} and M_{D_f} decrease, in average, 48% and 7%, respectively . The relative Df/DD mass contribution is higher than that found in BCN (13.5%) (see **Table 4**). The mean mass loading per episode is lower in comparison, representing a 35%, 44% and 36%, respectively, of that found in BCN for Dc, Df and DD particles. As stated before, this is consequence of the particular transport of dust intrusions to BCN and LPZ. These results reflect the fact, as stated before for the optical properties of dust particles (**Sect. 3.2.1**), that dust particles (Dc and Df components) are highly mixed with ND aerosols (Dc proportion is highly reduced) during the second dust episode at LPZ in comparison with the first one, which presented a well-differentiated dust layer between 3.5 and 5.5 km height with predominance of Dc particles (M_{D_c} of 78-84% is found for the most intense dust incidence period as occurred from 29 June 18UT to 30 June 02UT). In addition, these results are in accordance with **Sect. 3.1**, since the second dust event at LPZ corresponded to Saharan air masses coming directly from the Iberian Peninsula, when dusty conditions were still present, crossing Europe, thus allowing a higher dust mixing than that observed in BCN. However, for the first dust event at LPZ (when a defined high dust layer was observed), only air masses at higher altitudes experienced a pathway slightly crossing the Iberian Peninsula, but arriving at LPZ mainly without crossing Europe (see **Fig. 2**), avoiding thus a high degree of dust mixing.

As stated before, the dust intrusion arrived at BCN on 23 June. **Figure 4 (bottom panels)** shows that, in the night of 23-24 June, the CoM height of the dust intrusion reaches its highest value, i.e., Z_m is around 4 km. Regarding daily-averaged $\overline{Z_m}$ values for Dc and Df particles, the time evolution of their CoM heights follows a similar descending pattern from around 3 km height on 24 June down to 2 km on 30 June. Besides, $\overline{Z_m}$ for Df particles is slightly higher than that for the Dc component (200-250 m difference) on 27 June until the end of the dust event. These two results can indicate the removal of larger particles along with the progression of the dust intrusion over BCN.

In the case of LPZ, two consecutive, but different, dust episodes are observed. The first dust episode (a high well-defined dust layer) arrived at LPZ on 29 June at 11UT, mostly composed of Dc particles and with a CoM height of 4.6 km (slightly higher

with respect to BCN); then, it showed a constant descending evolution down to 3.7 km on 30 June at 05UT. Concerning the Df particles, their Z_m progression along this first episode is from 1.1 to 1.8 km height, peaking at 3.7 km on 29 June at 20UT. A mean $\overline{Z_m}$ value of 4.1 ± 0.3 and 3.0 ± 0.9 km is obtained, respectively, for the Dc and Df components during this dust episode. After that, a complete removal of the DD particles is observed. Later on 30 June, the dust signature is detected at 14UT again (second DD episode, with a high aerosol mixing, as regarded before), lasting until the end of that day (unfortunately, no P-MPL data were recorded later from 18UT). The CoM height also shows a descending behaviour, and the mean $\overline{Z_m}$ values during this episode for the Dc and Df particles are, respectively, 3.4 ± 0.1 and 3.1 ± 0.5 km height (slightly lower than those found on the first episode).

Therefore, as also mentioned before, differences in the vertical mass impact of the dust particles (their relative mass loading and CoM height) found in both distant BCN and LPZ locations are associated to the particular pathway of transported dust particles from the Saharan sources and between stations (see **Sect. 3.1**).

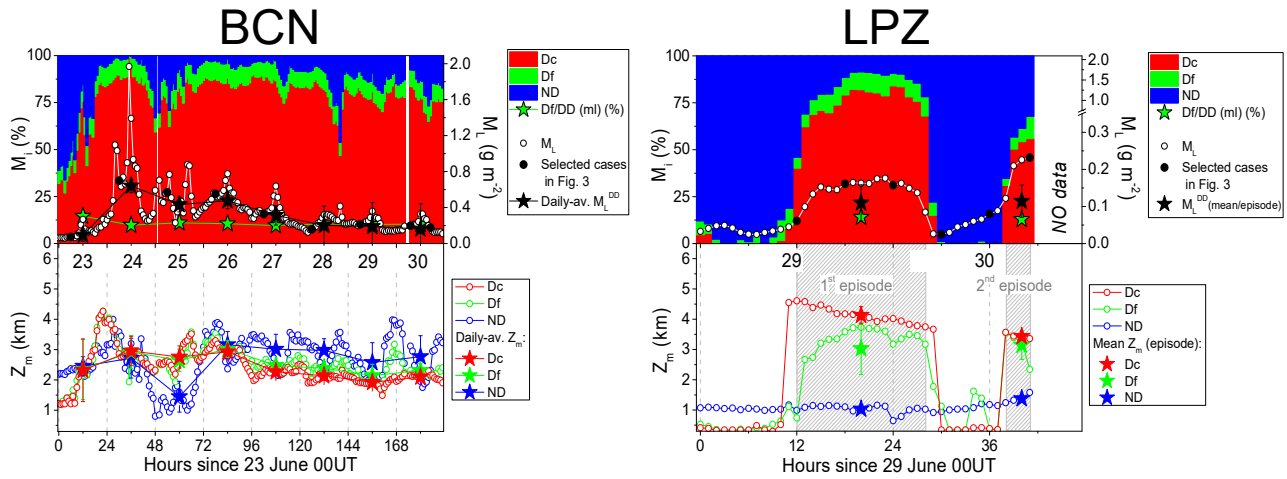

Figure 4: Evolution of the dusty events occurred at (Left) BCN and (Right) LPZ stations in June 2019 in terms of: (Top) the relative mass loading ratio (M_i, in %) for each component i: Dc (red), Df (green), and ND (blue), together with the total mass loading (M_L, g m^{-2}, white circles) and the daily-averaged/mean $\overline{M_L}$ values for the total dust ($\overline{M_L^{DD}}$; black stars); and (Bottom) the centre-of-mass (CoM) height, Z_m (km), for each component: Dc (red), Df (green) and ND (blue) together with their daily-averaged/mean values (full coloured stars, see legend). Black circles at the top panels indicate the representative profiles as shown in Fig. 3. White blanks represent either no retrieval achieved or no data available.

3.3 Dust direct radiative effect

This section is divided into four parts. The dust radiative properties as input data in the radiative transfer computations are introduced in **Sect. 3.3.1**. The direct radiative effect and radiative efficiency of dust particles, considered separately in both coarse and fine modes, on the surface (SRF), at the top-of-the-atmosphere (TOA) and in the overall atmospheric column (ATM) are presented in **Sects. 3.3.2 and 3.3.3**, respectively. In **Sect. 3.3.4**, the diurnal cycle of the dust direct radiative effect is examined.

3.3.1 Dust radiative properties

At the time of writing this article AERONET V3L2.0 data were available from BCN, while only V3L1.5 data were available from LPZ . **Figure 5** shows the time-height plot of the VLDR, δ^V, during the overall dust event period in BCN (23-30 June)

and LPZ (29-30 June) in the top panels, together with the AERONET AOD at 440 nm (AOD^{440}) and Ångström exponent ($AE_{440-870}$) at both sites in the bottom panels. AERONET AOD and Ångström exponent are given with an uncertainty of ± 0.02 (Eck et al., 1999), and ± 0.25, respectively, for $AOD^{440} > 0.1$ and in the order of 50% for $AOD^{440} < 0.1$ (Toledano et al., 2007).

According to the δ^V values plotted, the presence and the intensity of the dust outbreak in BCN is clearly visible, reaching a maximum 6-km height during the night of 23-24 June (marked as a white dashed line in **Fig. 5**). The dust plume top height remains pretty constant at around 6 km during the whole dusty period, while the vertical structure exhibits some variability. Although the dust event is still visible on 30 June, the intensity already starts decreasing from 27 June onwards. During 23-27 June the VLDR values below and above 1 km height are significantly different (less than 5% and greater than 10%, respectively) which could indicate that during that period the dust plume stayed aloft, decoupled from the local boundary layer. This fact can be confirmed by the vertical analysis of the optical properties, PBC and PLDR, as presented in **Sect. 3.2.1**, which highlights the location of the dust signature at altitudes between 1 and 6 km height (see **Fig. 3a**). In addition, the AOD^{440} reaches maximum values on 24 and 25 June, and starts decreasing afterwards. Inversely, $AE_{440-870}$ reaches minimum values on both 24 and 25 June and increases afterwards. AOD^{440} peaks at 0.63 on 25 June ($AE_{440-870}$ = 0.19); daily-averaged AOD^{440} values of 0.39 ± 0.07 and 0.35 ± 0.14 are found on 24 and 25 June, respectively.

In the case of LPZ, the event is less intense than in BCN and, as stated before, the dust intrusion occurs in two close but separated periods (see **Sect. 3.1**). AOD^{440} increases in the afternoon of 29 June (peaks at 0.15) while at the same time $AE_{440-870}$ drops from 1.5 down to 0.75. On 30 June AOD^{440} decreases in the morning and increases again in the afternoon up to a peak of 0.30 associated with values of $AE_{440-870}$ oscillating around 1.0.

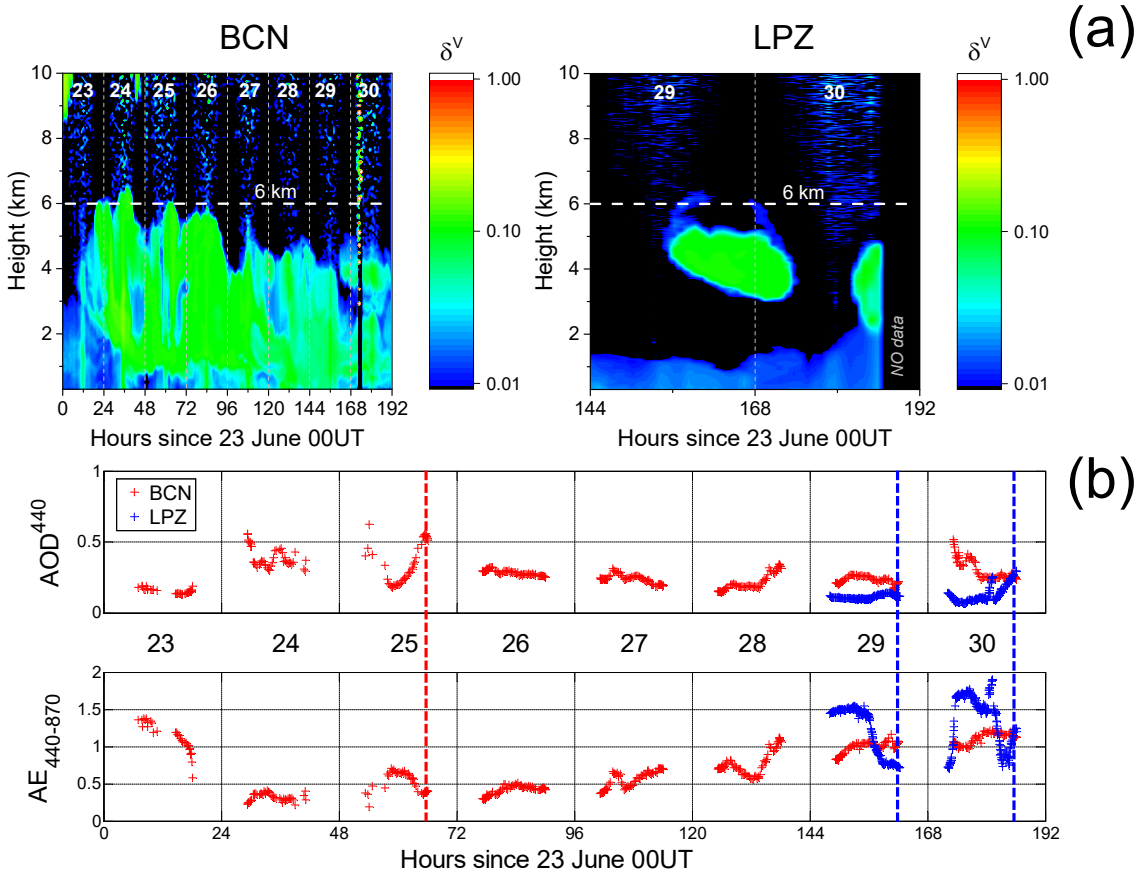

Figure 5: (Top) Time-height plot of the P-MPL VLDR, δ^V, in (Left) BCN and (Right) LPZ. (Bottom) AERONET AOD^{440} and $AE_{440-870}$, at BCN (red symbols) and LPZ (blue symbols) along the dust event period. The vertical red (BCN) and blue (LPZ)

dashed lines indicate the time corresponding to the AERONET representative values of the single scattering albedo (SSA), asymmetry factor (asyF) and surface albedo (SA) used in the RT simulations.

The dust radiative properties accepted by the GAME RT model are the AOD, the single scattering albedo (SSA) and the asymmetry factor (asyF). These three parameters should be spectrally defined for each height layer. The vertical profiles of dust coarse/fine mode extinction coefficient at 532 nm are obtained from the application of POLIPHON method to the continuous hourly-averaged P-MPL measurements (see **Sect.2.2**). These profiles are integrated along 18 layers, obtaining mean DOD values for both the coarse and fine mode. The spectral mean DOD value for each layer is calculated from the layer-mean DOD at 532 nm (DOD^{532}) using the AERONET $AE_{440-870}$. The SSA and asyF, as well as the surface albedo (SA), are available from AERONET database. These three properties are interpolated at the model wavelengths up to the highest AERONET wavelength (1020 nm) and assumed constant to the AERONET 1020-nm value beyond that limit. The asyF is given separately for the coarse and the fine mode. Since both available SSA and asyF are columnar variables, they are assumed constant with height. Because AERONET forces AOD > 0.4 for the retrieval of Level 2.0 SSA, AERONET V3L2.0 SSA are only available in BCN on 24 June (1 value in the morning) and 25 June (3 values in the afternoon). Hence, averaged DOD values on 25 June afternoon (noted 25 June-pm, red shaded line in **Fig. 5b**) are used to be representative of the whole event for BCN. Only AERONET V3L1.5 inversions are available at LPZ from both 29 and 30 June, at the moment of writing. Averaged afternoon values (noted 29Jpm and 30J-pm, blue shaded lines in **Fig. 5b**) are assumed as representative for each day. The same time intervals are considered for the SSA, asyF and SA. Their spectral dependence is represented in **Figure 6** and their corresponding values at 440 nm are reported in **Table 3**. AERONET SSA and asyF are given with an uncertainty of, respectively, ± 0.03 for $AOD^{440} > 0.5$ for dust and biomass burning, and ± 0.04 for desert dust particles (Dubovik et al., 2000; 2006).

Table 3: AERONET values at 440 nm of SSA, asyF and SA, for BCN on 25 June afternoon (25J-pm) and for LPZ on 29 and 30 June afternoon (29J-pm and 30J-pm, respectively). The mean DOD at 440 nm (DOD^{440}) in the same time interval is also included. Dc, Df and DD (Dc+Df) denote for dust coarse, dust fine and total dust aerosols, respectively.

		BCN, 25J-pm	LPZ, 29J-pm	LPZ, 30J-pm
DOD^{440}	Dc	0.212	0.056	0.041
	Df	0.052	0.027	0.026
	DD	0.264	0.083	0.067
SSA^{440}	DD	0.940	0.939	0.946
$asyF^{440}$	Dc	0.865	0.857	0.864
	Df	0.629	0.610	0.612
SA^{440}	DD	0.062	0.052	0.052

The SSA values found (approx. 0.94 at 440 nm, see **Fig. 6a**) are representative of moderately absorbing dust particles. The typical spectral behaviour of SSA for dust is expected to grow with increasing wavelength (Dubovik et al., 2002; Sicard et al., 2016). In the case of BCN, the SSA increases from 440 to 675 nm, with variations smaller than 0.01 beyond 675 nm. Given the high SSA values (0.98) for wavelengths greater than 675 nm and the estimated accuracy of this product (± 0.03, see Sicard et al., 2016), the spectral shape of SSA in BCN is that expected for dust. In the case of LPZ, SSA increases between 440 and 675 nm and decreases beyond 675 nm. This behaviour has been observed before by Sicard et al. (2016) for mixtures of dust

and pollution, when two opposite tendencies (dust SSA increases while pollution SSA decreases with increasing wavelength) combine. These results suggest that AERONET columnar observations in LPZ reveal a mixing of dust and, most probably, pollution particles. However, although the columnar SSA pattern is similar for both DD episodes, suggesting a certain dust-pollution mixing, lidar observations highlight the differences between those two episodes at LPZ: a well separated dust layer above 3.5 km height is observed for the first one, and a more mixed dust environment is found for the second one (as also stated in **Sect. 3.2**), both depending on the dusty air masses pathways reaching the LPZ station (see **Sect. 3.1**).

The spectral behaviour of the asymmetry factor is shown in **Figure 6b,** for both the coarse and the fine modes. The forward scattering is much more pronounced for large particles ($asyF^{440}$= 0.86) than for small particles ($asyF^{440}$ = 0.61-0.63), for all wavelengths. This result implies that, at constant AOD and low solar zenith angle (SZA), and independently of the wavelength, the solar radiation scattered to the surface is greater for the coarse mode than for the fine mode. The spectral asyF decreases with increasing wavelength for both modes, being similar for the coarse mode in BCN and LPZ. This indicates that the scattering properties of this mode will have a similar effect on the radiative effect retrievals at both sites. If the coarse mode in the column is formed exclusively of dust particles, it can be stated that the aging of dust has no effect on the absorption capabilities of the coarse mode. The forward scattering of the fine mode at wavelengths greater than 675 nm is slightly higher at BCN ($asyF^{675}$ = 0.59) than at LPZ ($asyF^{675}$ = 0.52). This result implies that, at near-infrared wavelengths (> 675 nm), for constant AOD and low SZA, the solar radiation scattered to the surface by fine particles should be greater at BCN than LPZ.

The surface albedo shows (see **Fig. 6c**) a general growing trend with increasing wavelength. Similar SA values are found at both sites at 440 ($0.05 < SA^{440} < 0.06$) and 675 nm ($0.09 < SA^{675} < 0.11$). At wavelengths larger than 870 nm higher SA values are found in LPZ (SA^{870} = 0.34) than in BCN (SA^{870} = 0.25), indicating that at near-infrared wavelengths the surface will appear “brighter” at LPZ as compared to BCN, and accordingly, at constant incoming radiation reaching the surface, more radiation will be reflected upward in LPZ than in BCN. The spectral values found of the surface albedo are similar to those reported in Granados-Muñoz et al. (2019), which were measured in Granada, Spain, at the same period of the year.

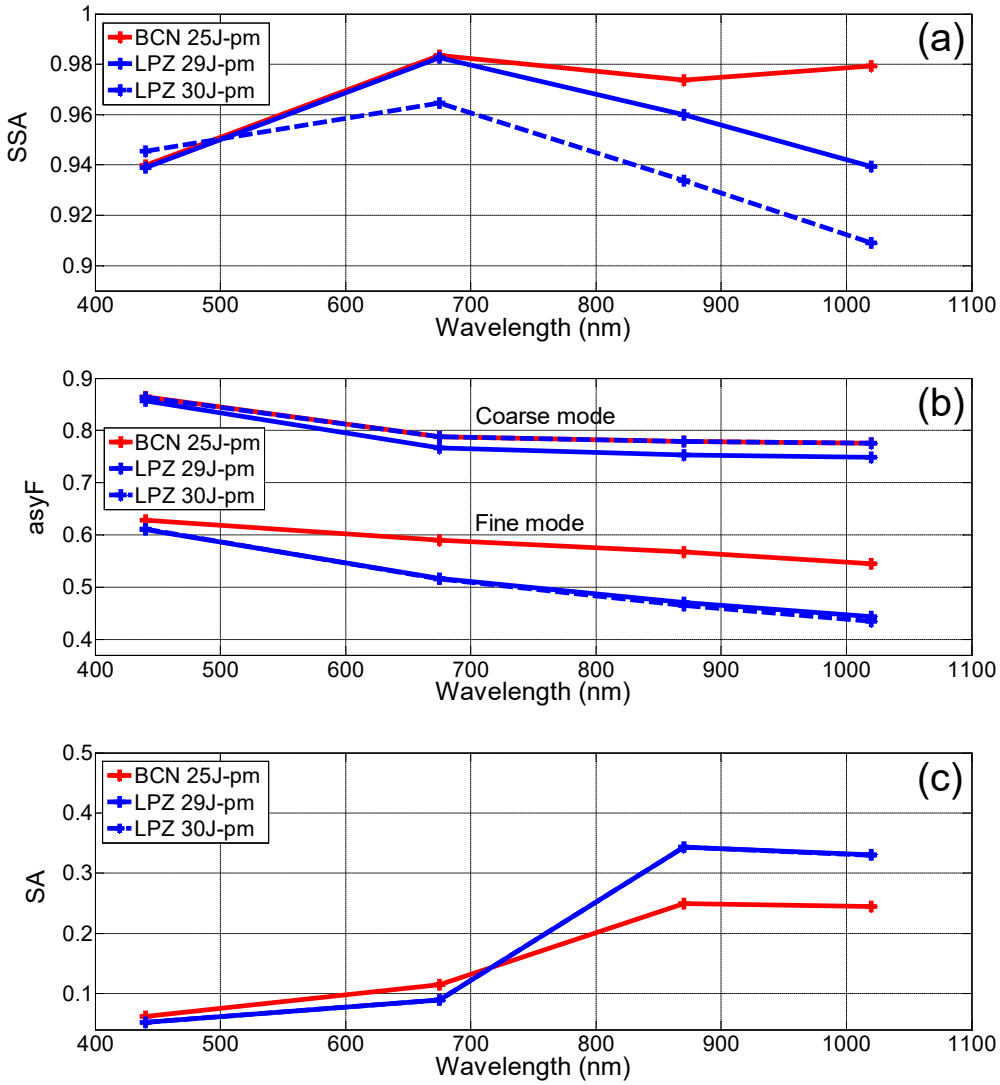

435

Figure 6: AERONET spectral behaviour of (a) SSA, (b) asyF and (c) SA for BCN (red lines) on 25 June afternoon (25J-pm) and for LPZ (blue lines) on 29 and 30 June afternoon (29J-pm, solid lines, and 30J-pm, dashed lines, respectively).

3.3.2 Dust direct radiative effect on the surface

440 GAME simulations were performed for the 8 days considered in BCN (23-30 June) and the two days in LPZ (29-30 June), each day from 05 to 19UT, when the sun was above the horizon (SZA < 90º). The shortwave dust direct radiative effect (DRE) was calculated by using **Eqs. 9** and **10**, and is plotted separately for the dust coarse (Dc) and fine (Df) modes plus the combined effect (DD=Dc+Df) in **Figure 7**. The fine-to-total ratio (Df/DD) was also calculated for both the DOD and DRE. The instantaneous dust radiative efficiency (DREff) was calculated as the ratio of instantaneous DRE to DOD and the daily DREff
445 as the best linear fit forced to 0 of the scatterplot of instantaneous values of one full day of DRE as a function of DOD (see explanations in next paragraphs). Daily and maximal instantaneous values of DRE and DREff on the surface are shown in **Table 4**.

For both size modes the dust direct radiative effect on the surface (SRF), $DRE(SRF)$, is negative for the overall dusty period (see **Fig. 7**, blue bars), indicating an aerosol cooling of the surface. In BCN, most of the instantaneous coarse (fine) mode
450 DRE, DRE_{Dc} (DRE_{Df}), are above -20 W m^{-2} (-10 W m^{-2}). These values suggest that in terms of instantaneous radiative effect,

the dust event should be classified as moderate. The singular aspect of the event lies in its duration and geographical extension. Instantaneous values of the total DRE, DRE_{DD}, below -20 W m^{-2} are reached during four days from 24 to 27 June, which can be identified as the most intensive period of the event in BCN (the daily DOD at 532 nm, DOD^{532}, varies between 0.13 and 0.26), as stated before in **Sect. 3.2**. Peak values of the instantaneous DRE are reached at the same time for both modes on 25 June at 17UT and produce a peak of total DRE of -54.5 W m^{-2} (DOD^{532} = 0.45). This maximum is in the range of values as calculated by Sicard et al. (2014a) (-55.4 - -53.1 W m^{-2}) for two mineral dust outbreaks occurred in Barcelona in summer 2009 and AODs of 0.38. In terms of daily-averaged values (see **Table 4**), DRE_{Dc} and DRE_{Df} were -5.7 ± 2.8 and -3.4 ± 1.3 W m^{-2} in average over the whole event (23-30 June), leading to a daily DRE_{DD} of -9.1 ± 3.9 W m^{-2}. For comparison, Meloni et al. (2005) found daily values of DRE in the central Mediterranean of -6.7 W m^{-2} (AOD^{550} = 0.227; SSA^{440} = 0.96 and asyF^{440} = 0.80) and -10.2 W m^{-2} (AOD^{550} = 0.227; SSA^{440} = 0.88 and asyF^{440} = 0.81). Compared to climatological values, our findings are also in agreement with recent works reporting about the same region. For instance, Tsikerdekis et al. (2019) simulated with RegCM4 the dust shortwave direct radiative effect for a 10-year period (01 December 1999 to 30 November 2009) and found for the summer season values of -14.9 and -5.5 W m^{-2} over the Sahara region and for the Mediterranean Basin, respectively. The fine-to-total ratio (Df/DD) of the daily DRE varies between 28 and 46%, being 37% in average over the whole dust event, that is, the Df/DD ratio of DRE produce a little more than one third of the total DRE. This result can be interestingly related to the Df/DD ratio of the daily DOD (24%), meaning, in relative terms, that the dust fine particles contribute more to the total DRE than they do to the DOD.

Figure 8 nicely illustrates the dust direct radiative effect on the surface, $DRE(SRF)$, and at the TOA, $DRE(TOA)$. **Figure 8a** shows the instantaneous $DRE(SRF)$ for both coarse (red) and fine (blue) modes as a function of their respective DOD^{532}. By using linear regression analysis (regarding DRE=0 with DOD=0), the DREff corresponds to the slope of the linear fittings. In BCN, the total dust DREff on the surface, $DREff(SRF)$, over the whole event is -75.2 and -129.6 W m^{-2} τ^{-1}, for the coarse and fine mode respectively, producing a total dust DREff of -88.9 ± 4.3 W m^{-2} τ^{-1}. Note the small deviation of the cloud of points from the linear fitting (± 2.9 and ± 1.4 W m^{-2} for the coarse and fine mode, respectively). It can be clearly seen that at constant DOD the dust fine mode produces a higher enhancement of DRE than the dust coarse mode. Both DRE and DREff values are included in **Table 4**.

The main difference between the parametrizations for the radiative properties of both modes is the asymmetry factor: asyF values of 0.865 and 0.629 are reported for the coarse and fine modes, respectively. The lower asyF value found for the fine mode with respect to the coarse one implies that, in relation to a pure forward-scattering particle, more solar irradiance is scattered in the atmosphere by Df particles and thus less irradiance is reaching the surface. Another difference is the vertical distribution of each of those coarse- and fine-mode dust layers. However, the height of the dust layer is not expected to have a relevant impact on the $DRE(SRF)$ (Liao et al., 1998).

During the most intensive days of the event in BCN, 24-27 June, the total dust $DREff(SRF)$ varies between -100.3 and -87.9 W m^{-2} τ^{-1}. For comparison, measurements of the daily total dust DREff on the surface in the central Mediterranean of -86.4 ± 5.3 W m^{-2} τ^{-1} are reported by Di Sarra et al. (2008) for an AOD of 0.35 as averaged over two summer solstices (2003-2004), and -85.3 ± 4.7 W m^{-2} τ^{-1} are obtained by Di Biagio et al. (2009) for an AOD of 0.33 as averaged over three summer solstices (2005-2007). Lyamani et al. (2006) found in south-eastern Spain values of total dust daily DREff of -73.4 W m^{-2} τ^{-1} for dust mixed with biomass burning during the 2003 heat wave with an AOD varying in the range 0.4 - 0.6. Closer to the dust source, in northern Benin, Mallet et al. (2008) calculated for a few days of clear-sky dust intrusion in January 2006 mean daily $DRE(SRF)$ values of -61.5 W m^{-2} and mean daily DREff of -57.9 W m^{-2} τ^{-1} (mean AOD of 1.06). This short literature review does not intend to be exhaustive. However, it might lead to consider that, as mineral dust direct radiative effect decreases with horizontal transport, the dust radiative efficiency might, inversely, increase as the mineral dust moves away from its source. More elements of discussion on this topic are brought in two paragraphs further.

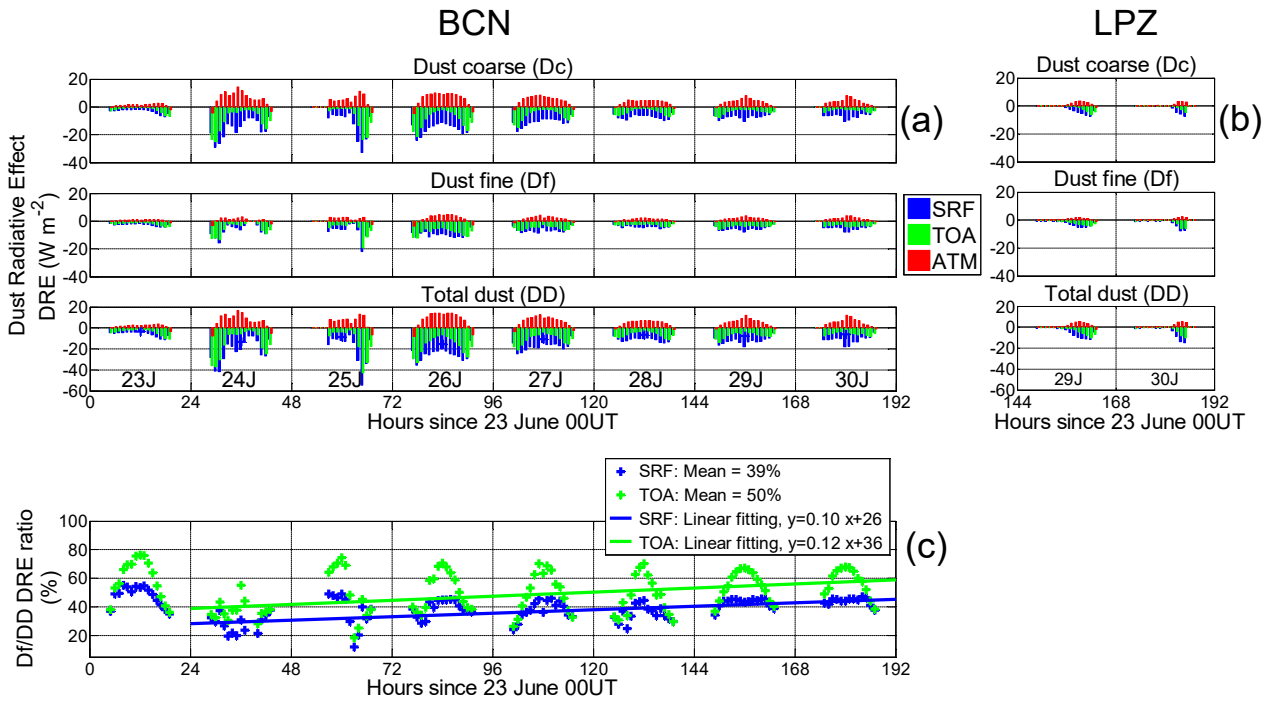

Figure 7: Instantaneous dust direct radiative effects (DRE) on the surface (SRF) (blue), TOA (green) and in the atmosphere (red) in (a) BCN and (b) LPZ. (c) Fine-to-total (Df/DD) ratio of the instantaneous dust DRE on the surface (SRF) and at the TOA in BCN; the best linear fit has been calculated between 24 and 30 June (i.e., discarding 23 June) (both mean values and linear fittings are included in the legend). The absolute increase of Df/DD DRE ratio on SRF (TOA) of +0.10 (+0.12)%·hr^{-1} is equivalent to an increase of +2.4 (+2.9)%·day^{-1}.

In LPZ, the event is much weaker than in BCN. Under dusty conditions, the DOD is, respectively, 0.083 and 0.067 (see **Table 3**) for the first (from 29J-pm to 30J-am) and second (30J-pm) dust episodes. On both days, the fine-to-total (Df/DD) ratio of the DOD is approximately of one-third (one-fourth in BCN). The dust instantaneous DRE is on the order of magnitude of the DRE in BCN on the first weak day of the outbreak (23 June), with peaks of -7.4 and -7.8 W m^{-2} for the coarse and fine mode, respectively (see **Fig. 7**). The daily DRE, as averaged over the two days, is -1.2 ± 0.4 and -1.3 ± 0.2 W m^{-2} for the coarse and fine mode, respectively, yielding to a total dust DRE of -2.5 ± 0.6 W m^{-2};in particular, the radiative contribution of the Df particles was of 52% with respect to DRE_{DD} (37% in BCN). Despite the radiative impact of the mineral dust in LPZ is small (because of the low dust loading), this result is remarkable. It shows that, under some given circumstances, dust fine mode contribution to the DRE is comparable to that of the coarse mode, whereas mineral dust is usually regarded as a coarse-dominating aerosol. The increase of the Df/DD ratio of daily DRE in LPZ (52%) with respect to BCN (37%) is due to the gravitational settling of the largest dust particles during a longer transport to LPZ. Indeed, according to **Section 3.1,** dust particles arriving at LPZ on 29 and 30 June at 4500 m height were travelling over the Iberian Peninsula for 3-4 days before (see **Fig. 2**). In terms of radiative efficiency, the $DREff_{Dc}$ and $DREff_{Df}$ in LPZ, as averaged over the two days 29 and 30 June, is, respectively, -89.5 and -157.9 W m^{-2} τ^{-1} (slightly higher, in absolute value, than in BCN, that is, -75.2 ± 2.9 and -129.6 ± 1.4 W m^{-2} τ^{-1}, respectively; see **Fig. 8a** and **Table 4**). Note again the small deviation of the cloud of points from the linear fitting (± 0.8 and ± 0.5 W m^{-2} for the coarse and fine mode, respectively).

There are two main differences between BCN and LPZ parametrizations: the spectral asyF is slightly larger in BCN than in LPZ (see **Fig. 6b**) and the spectrally-integrated SA is lower in BCN than in LPZ (see **Fig. 6c**). At constant DOD, both differences have an opposite impact on the dust DRE on the surface: the first one (higher asyF in BCN) will yield a weaker cooling effect (i.e. a larger radiative efficiency, as indeed observed), while the second one (smaller SA in BCN) will yield a stronger cooling (unlike what is observed). The effect of the higher spectral asyF in BCN is thus dominating over the effect caused by a lower albedo. The SA variation has indeed a small impact in the $DRE(SRF)$. Osipov et al. (2015) showed that a SA decrease from 0.35 to 0.25 (which is approximately the difference in SA between LPZ and BCN at the near-infrared wavelengths; see **Fig. 6c**) yields to a difference in the SW DRE on the surface less than 3 W m^{-2}.

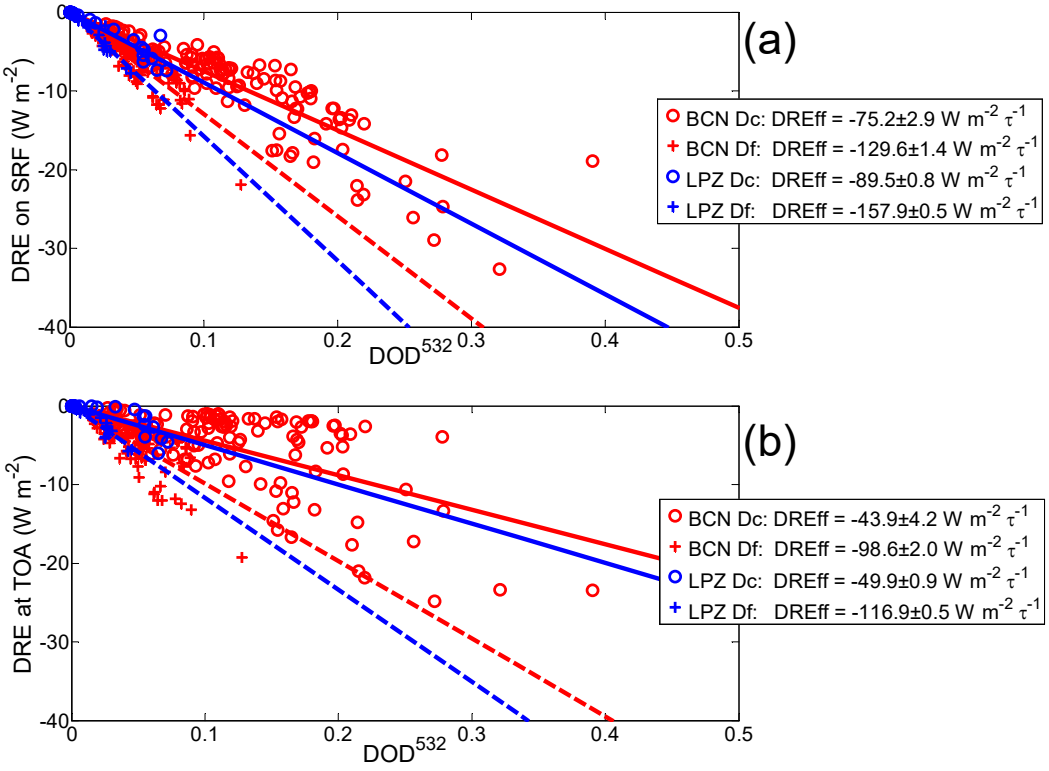

Figure 8: Dust direct radiative effect (DRE) (a) on surface (SRF) and (b) at TOA as a function of DOD at 532 nm (DOD^{532}), as shown separately for the dust coarse (Dc, circles, solid lines) and dust fine (Df, crosses, dashed lines) components at both BCN (23-30 June) (in red) and LPZ (29-30 June) (in blue). Corresponding DREff values (slope of the linear fitting: DRE vs. DOD) are included in the legend, as well as their standard deviation (i.e., the standard deviation of the points from the best linear fit).

In addition, the time evolution of the instantaneous Df/DD DRE ratio is shown in **Figure 7c** for BCN. On the surface, this ratio (in blue) shows a diurnal cycle, whose shape changes from day-to-day. The mean DRE value over the whole dust event of these instantaneous Df/DD ratios on the surface is 39%. By discarding the first day (23 June) when the dust arrived at BCN, an increase of the Df/DD DRE ratio with time can be observed. The best linear fit as calculated between 24 and 30 June presents a positive slope, i.e. an absolute increase, of +0.10%·hr^{-1}, that is, +2.4%·day^{-1}. In other terms, the contribution of the dust fine mode to the total dust DRE on the surface increases steadily along the dust event, being the increase of +16% between the beginning of the event (on average, 28% on 24 June) and its end (44% on 30 June).

3.3.3 Dust direct radiative effect at TOA and in the atmosphere

Both the DRE and DREff at the TOA, $DRE(TOA)$ and $DREff(TOA)$, are calculated, similarly as on the surface. The radiative effect of dust in the atmosphere, $DRE(ATM)$, as defined in **Eq. 10,** is also obtained. The time evolution of the instantaneous dust DRE at TOA is shown in **Figures 7a** (BCN) and **7b** (LPZ) and in dependence of DOD in **Figure 8b.** Daily and maximal values are reported in **Table 5**.

In BCN, the DRE at TOA is negative along all the dusty period. The overall mean daily DRE at TOA is -3.2 ± 1.8 and -2.6 ± 1.1 W m^{-2} for the coarse and fine mode, respectively, being their instantaneous maxima of -24.8 (24 June) and -19.3 W m^{-2} (25 June). For the total dust, the overall mean daily $DRE_{DD}(TOA)$ was -5.8 ± 2.8 W m^{-2}, and an instantaneous maximum of -42.7 W m^{-2} was reached on 25 June. For the coarse mode, the instantaneous dust DRE at TOA ($DRE_{Dc}(TOA)$, green bars in **Fig. 7a**) was smaller than that on the surface (in terms of daily values, $DRE_{Dc}(TOA)$ represented 56% of that found on the surface). For the fine mode, this difference is less pronounced: $DRE_{Df}(TOA)$ represents 76% of the surface value. The lower ratio of $DRE(TOA)$ to $DRE(SRF)$ for Dc particles (as compared to Df ones) is mostly due to the strong forward-scattering property of large particles (asyF(Dc) > asyF(Df)), as associated to the fact that the surfaces considered are not especially bright (see **Fig. 6c**). Comparing with values found in the literature, the daily $DRE(TOA)$ values obtained in this work are higher, in absolute value, than those found in Europe ([-3.6, -2.2 W m^{-2}], Meloni et al., 2005; -4.0 W m^{-2}, Lyamani et al., 2006) but similar to values found in northern Benin (~-5.0 W m^{-2} for AOD ~ 0.30-0.35, Mallet et al., 2005). In terms of instantaneous values, absolute peak values are higher to most of those found in the literature (-8.7 W m^{-2}, Meloni et al., 2005; -24.6 W m^{-2}, Sicard et al., 2014a; -10.3 W m^{-2}, Granados-Muñoz et al., 2019). This difference is probably due to different aerosol loadings: the AOD associated to the maximum of $DRE(TOA)$ found in this study (AOD=0.56 on 25 June at 17:30UT, see **Fig. 5**) is much higher than those reported in the mentioned references. The instantaneous maximum as calculated for $DRE(TOA)$, -42.7 W m^{-2}, is, for instance, close to the values within the range [-55.0, -50.0 W m^{-2}] as found by Cachorro et al. (2008) for a dust event and AODs varying in the range [0.82, 1.04]. The fine-to-total (Df/DD) ratio of the daily $DRE(TOA)$ in BCN varies between 36 and 56%, being 45% in average over the whole dust event. This ratio is higher than that found on the surface (37%).

In LPZ, the DRE at the TOA, $DRE(TOA)$, is, in absolute value, much lower than in BCN. The mean total dust daily $DRE(TOA)$ value is -1.5 ± 0.4 W m^{-2}, reaching an instantaneous maximum of -10.3 W m^{-2}. In terms of daily values, $DRE_{Dc}(TOA)$ and $DRE_{Df}(TOA)$ in LPZ represents 50 and 70%, respectively, of that found on the surface. This difference in daily DRE of 20% between the dust coarse- and fine-mode is the same than that observed in BCN, and the reasons for it are those already mentioned. The Df/DD DRE ratio at TOA ranges between 56 and 67%, being 60% in average for the two dust episodes. In addition, similarly to BCN, that value is higher than that obtained on the surface (52%).

These results indicate that, likewise on the surface, Df particles contribute more to the total $DRE(TOA)$ in LPZ than in BCN because of the gravitational settling of the largest dust particles during a longer transport, as stated before (see **Sect. 3.1**), and that, in relative terms, their contribution is stronger at the TOA than on the surface. This result is especially relevant for satellite remote sensing instrumentation, which is mostly sensitive to SW wavelengths, since its measurements can be likely affected by dust contamination (Marquis et al., 2021).

Since the DRE is lower at the TOA than on the surface, the $DREff$ at the TOA consequently decreases as compared to that on the surface. This is shown in **Figure 8,** where the slope of the best linear fitting is less steep at the TOA than on the surface, i.e. $DREff(TOA)$ is negatively higher than $DREff(SRF)$. In BCN the daily $DREff_{Dc}(TOA)$ and $DREff_{Df}(TOA)$, as averaged over the whole dust event, are -43.9 ± 4.2 and -98.6 ± 2.0 W m^{-2} τ^{-1}, respectively, showing a deviation of the cloud of points from the linear fitting still low for both the coarse and fine mode, but higher than at the surface (± 2.9 and ± 1.4 W m^{-2}, respectively). The total dust $DREff_{DD}(TOA)$ is -58.0 ± 6.2 W m^{-2} τ^{-1}. Since $DREff$ is an intensive parameter, those values can be compared to instantaneous dust $DREff$ found in the literature, obtaining relatively similar values within a

certain interval. For instance, Sicard et al. (2016) measured a summer-mean aerosol $DREff(TOA)$ of -70.8 ± 16.8 W m^{-2} τ^{-1} in Palma de Mallorca (Balearic Island) and of -90.0 ± 9.1 W m^{-2} τ^{-1} in Ersa (Corsica Island) over a period of 5 years between 2011 and 2015. During a strong dust intrusion at Lampedusa, reaching AOD values of 0.6, Meloni et al. (2015) found an $DREff(TOA)$ approximately -77 W m^{-2} τ^{-1}. In LPZ, the $DREff(TOA)$, in absolute values, are higher than in BCN, that is, -49.9 ± 0.9, -116.9 ± 0.5 and -73.4 ± 1.4 W m^{-2} τ^{-1} are found, respectively, for Dc and Df particles and the total dust (DD). Daily and maximal instantaneous values of DRE and DREff at the TOA are shown in **Table 5**.

Results concerning the dust radiative effect in the atmospheric column, $DRE(ATM)$, are reported in **Figures 7** and **9**. The statistics of the event is not reported to avoid an excessive length of the paper. Daily $DRE(ATM)$ and $DREff(ATM)$ can be easily calculated by subtracting the DRE and $DREff$ values as obtained at the TOA (**Table 5**) and those found on the surface (**Table 4**) (see **Eq. 10**). **Figure 7** shows that the dust produces generally a heating of the atmosphere (most of the red bars are positive in **Fig. 7**). The daily Dc, Df and DD $DRE(ATM)$ in BCN are, respectively +2.5 ± 4.5, +0.8 ± 2.4 and +3.3 ± 6.8 W m^{-2}, being slightly lower in LPZ (+0.6 ± 0.6, +0.4 ± 0.4 and +1.0 ± 1.0 W m^{-2}, respectively). The Df/DD ratio of $DRE(ATM)$ is 24% in BCN, and higher in LPZ (40%). These values are surprisingly very similar to the Df/DD ratio of DOD (24% in BCN and 38% in LPZ). This finding, together with the results of **Section 3.3.2**, indicates that the Df particles (dust fine mode) have a lower impact on the overall atmospheric column than on the surface and at the TOA. In terms of radiative efficiency, the Dc, Df and DD mean daily values of $DREff(ATM)$ over the whole dust event in BCN are +31.3 ± 7.1, +31.0 ±3.4 and +30.9 ± 10.5 W m^{-2} τ^{-1}, respectively; those values are higher in LPZ: +39.6 ± 1.7, +41.0 ± 1.0 and +40.0 ± 2.7 W m^{-2} τ^{-1}.

The difference between BCN and LPZ may be the result of a lower SSA and a higher SA at near-infrared wavelengths in LPZ than in BCN: both effects produce a smaller $DRE(TOA)$ in absolute value, and thus a higher $DREff(ATM)$. Interestingly the dust radiative efficiency in the atmospheric column is virtually independent of the dust mode at both BCN and LPZ. However, due to the complexity of the mechanisms involved and the characteristics of the particles observed, those results are likely a coincidence and do not apply further than in our singular case. Similar total dust $DREff(ATM)$ are reported in the literature, e.g., by Derimian et al. (2008) who found values of +40.6 W m^{-2} for an AOD~0.54 measured in Senegal. However, larger values are also often reported; for instance, Lyamani et al. (2006) found values of +58.9 W m^{-2} (AOD ~ [0.4 - 0.6]) in Granada (Spain), and Sicard et al. (2012) obtained values of +101.0 W m^{-2} (AOD~0.59) for strongly absorbing dust particles in Barcelona. As compared to the later, dust $DREff(ATM)$ values found in this work are smaller. The reason relies on the dust $DRE(TOA)$ is unusually large, in absolute value, because of the relatively strong contribution of the Df particles at both sites.

Finally, the time evolution of the instantaneous Df/DD $DRE(TOA)$ ratio in BCN must be commented. That ratio at the TOA (see **Fig. 7c,** in green) shows a strong inverted U-shaped diurnal cycle with values almost double at central hours of the day as compared to dawn/dusk. The mean value over the whole dust event of Df/DD $DRE(TOA)$ ratio is 50%. By discarding the first day (23 June), an increase of the Df/DD DRE ratio at TOA with time is observed, being stronger than that on the surface (see **Fig. 7c,** in blue). The best linear fit, calculated with data from 24 to 30 June presents a positive slope, i.e. an absolute increase, of +0.12%·hr^{-1}, i.e. +2.9%·day^{-1}. On average, the contribution of the Df particles to the total dust DRE at the TOA is +20% higher between 24 June (36%) and 30 June (56%). Likewise, a slightly smaller positive slope of +0.10%·hr^{-1} (i.e.,+2.4%·day^{-1}, see **Sect. 3.3.2**) is found for the Df/DD DRE ratio on the surface, which is +16% higher between 24 June (28%) and 30 June (44%).

3.3.4 Diurnal cycle of the dust direct radiative effect

In order to analyse the diurnal cycle of DRE, June 26th at BCN is selected, since the dust plume vertical distribution is relatively stable and the AOD is almost constant along that day (see **Fig. 5**). The diurnal cycle of the Dc, Df and DD DRE on the surface, at TOA and in the atmospheric column is represented in **Figure 9** and it can be described as singular, especially for the ground

level (SRF). Cooling occurs at both the surface and TOA for all modes (Df, Dc and DD) and at all hours of the day. The dust (all modes) produces a heating of the atmosphere during the most of hours of the day and a slight cooling (i.e., $|DRE(TOA)| > |DRE(SRF)|$) close to dawn/dusk. At both the surface and TOA, the shape of the diurnal cycle of DRE_{Dc} and DRE_{DD} is similar to a "W", showing two minima, one in the morning (around 06UT) and one in the afternoon (17-18UT), and a maximum at central hours of the day. These results are explained by the sensitivity analysis of SSA, asyF and SA upon the shape of the diurnal DRE cycle as performed by Osipov et al. (2015), and also by a former study of Osborne et al. (2011). The "W" shape, called MMM (min-max-min) structure by Osipov et al. (2015), is basically due to a combination of solar geometry and dust anisotropic scattering: even though the direct radiative effect produced by forward-scattering particles increases with increasing solar zenith angle, the decreasing solar irradiance for long slant paths (at dawn and dusk) causes those actual valleys as achieved at intermediate solar zenith angles (Osborne et al., 2011). This is valid at both the surface and TOA. For high values of asyF, increasingly pronounced MMM structures are expected (Osipov et al., 2015). Independently of the particle size, Osborne et al. (2011) also showed that spheroids produce greater asyF values than spheres or irregular-shaped particles, and thus accentuating the MMM structure. The diurnal DRE_{Df} cycle does not show this MMM structure, remaining nearly constant along the day. Additionally it must be pointed out that $DRE_{Df}(SRF)$ and $DRE_{Df}(TOA)$ are of the same order of magnitude, and the daily $DRE_{Df}(ATM)$ (+1.3 W m^{-2}) is low enough, indicating that Df particles produce a quasi-neutral radiative effect on the overall atmospheric column. The decrease of DRE_{Dc} on the surface (at TOA) between the central hours of the day and dawn/dusk is -10.5 (-16.9) W m^{-2}, which, once summed to the DRE_{Df}, induces a decrease in the DRE_{DD} of -13.3 (-23.7) W m^{-2}. The diurnal DRE variations at TOA are larger than on the surface, a result also observed by Osborne et al. (2011). As a consequence, $DRE(ATM)$, the difference between $DRE(TOA)$ and $DRE(SRF)$, for both Dc and DD, showed the shape of an inverted U. In the central hours of the day $DRE_{Dc}(TOA)$ is approaching zero (-1.9 W m^{-2} at 12UT). It would have become positive if, for example, asyF had been higher, or if the dust had been more absorbing (i.e., SSA < 0.94), or if the surface had been more reflective. It is worth noting that this MMM structure is not an intrinsic characteristic of the diurnal DRE cycle as induced by mineral dust. Banks et al. (2014) found a mean daytime cycle of dust DRE on the surface in the Algeria (central Sahara; AOD ~ 1, SSA ~ 0.977) peaking toward local noon and decreasing (in absolute value) at both the beginning and the end of the day; they also found a mean daytime DRE cycle at TOA with a MMM structure and positive peak values in the central hours of the day. These two behaviours were reproduced by the sensitivity study of Osipov et al. (2015): for pure forward-scattering particles (asyF = 1) in the first one, and for bright surfaces (from desert to white body) in the second one.

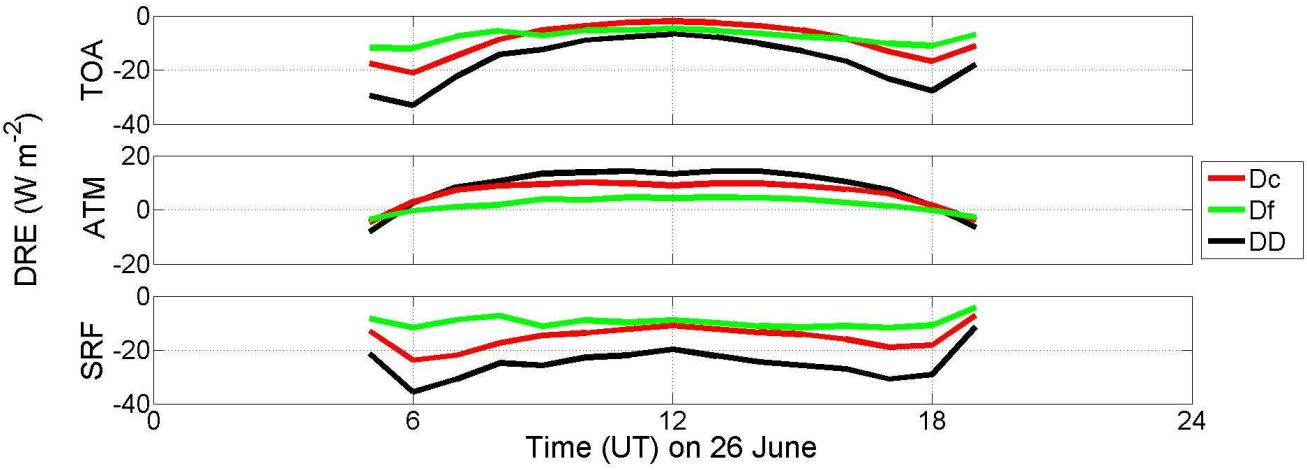

Figure 9: Diurnal cycle on 26 June in BCN of the dust direct radiative effect DRE (Bottom) on the surface (SRF), (Centre) in the atmosphere (ATM), and (Top) at TOA. The daily-mean AOD^{440} for Dc and Df particles is, respectively, 0.19 ± 0.02 and 0.06 ± 0.02;

SSA^{440} is taken constant to 0.94; $asyF^{440}$ is also taken constant but is different for both modes: 0.865 and 0.629 for coarse and fine

655 **modes, respectively.**

Table 4: DRE (W m^{-2}) and DREff (W m^{-2} τ^{-1}) on the surface (SRF) as induced by Dc, Df and DD particles along the particular dust periods in BCN and LPZ. $\bar{X}$ and $X(max)$ indicates daily-averaged and maximal instantaneous values, respectively. The daily DOD at 532 nm (DOD^{532}) and the mass loading (m_L, in g m^{-2}) are also included. D_f/DD denotes the Df-to-total dust ratio.

		BCN									LPZ (*)		
June 2019		23	24	25	26	27	28	29	30	23-30	29	30	29-30
DOD^{532}	$\overline{D_c}$	0.055	0.189	0.098	0.193	0.140	0.090	0.092	0.071	0.116	0.028	0.020	0.024
	$\overline{D_f}$	0.019	0.041	0.031	0.062	0.045	0.029	0.039	0.031	0.037	0.016	0.013	0.015
	$\overline{DD}$	0.074	0.230	0.129	0.255	0.185	0.119	0.131	0.102	0.153	0.044	0.033	0.039
	$\overline{D_f}/\overline{DD}$ (%)	26	18	24	24	24	22	30	30	24	36	39	38
m_L	$\overline{D_c}$	0.083	0.585	0.386	0.425	0.284	0.181	0.169	0.145	0.282	0.098	0.099	0.098
	$\overline{D_f}$	0.012	0.055	0.047	0.050	0.030	0.021	0.020	0.017	0.032	0.012	0.015	0.014
	$\overline{DD}$	0.095	0.640	0.434	0.476	0.314	0.202	0.188	0.162	0.314	0.110	0.114	0.112
	$\overline{D_f}/\overline{DD}$ (%)	14.5	10	11	10.5	9.5	10	10	10	11	14	13	13.5
DRE	$\overline{D_c}$	-2.0	-9.6	-5.7	-9.5	-6.8	-4.4	-4.4	-3.4	-5.7	-1.4	-0.9	-1.2
	$D_c(max)$	-7.0	-29.0	-32.6	-23.9	-17.6	-9.6	-9.7	-10	-32.6	-7.4	-7.4	-7.4
	$\overline{D_f}$	-1.7	-3.7	-3.2	-6.1	-4.1	-2.4	-3.3	-2.7	-3.4	-1.4	-1.1	-1.3
	$D_f(max)$	-4.5	-15.6	-21.9	-11.7	-8.6	-5.3	-6.6	-8.0	-21.9	-5.0	-7.8	-7.8
	$\overline{DD}$	-3.7	-13.3	-8.9	-15.6	-10.9	-6.8	-7.7	-6.1	-9.1	-2.8	-2.0	-2.5
	$DD(max)$	-11.3	-41.8	-54.5	-35.6	-24.5	-14.5	-17.9	-18	-54.5	-11.7	-14.6	-14.6
	$\overline{D_f}/\overline{DD}$ (%)	46	28	36	39	38	35	43	44	37	50	55	52
DREff	$\overline{D_c}$	-73.4	-75.3	-85.9	-78.5	-72.5	-66.5	-66.9	-62.2	-75.2	-86.1	-95.6	-89.5
	$D_c(max)$	-116.3	-113.3	-105.4	-111.0	-116.4	-103.6	-104.2	-103	-116.4	-115.1	-107.0	-115.1
	$\overline{D_f}$	-123.0	-145.5	-143.9	-133.4	-124.8	-111.0	-119.1	-112.3	-129.6	-148.8	-167.6	-157.9
	$D_f(max)$	-176.7	-181.0	-173.6	-181.7	-188.5	-158.2	-161.9	-157	-188.5	-188.7	-172.1	-188.7
	$\overline{DD}$	-89.3	-87.9	-100.3	-93.4	-86.2	-77.5	-82.7	-77.7	-88.9	-106.6	-123.5	-113.4
	$DD(max)$	-133.7	-129.8	-121.5	-128.3	-130.3	-114.6	-121.7	-120.0	-133.7	-153.9	-147.7	-153.9

(*) 29 and 30 June represent the first and second DD episode, respectively, as observed in LPZ.

Table 5: Idem as Table 4, but at the TOA. DOD^{532} values are shown in Table 4.

		BCN									LPZ (*)		
June 2019		23	24	25	26	27	28	29	30	23-30	29	30	29-30
DRE	$\overline{D_c}$	-1.3	-5.8	-3.4	-5.7	-3.7	-2.3	-2.1	-1.4	-3.2	-0.8	-0.4	-0.6
	$D_c(max)$	-6.8	-24.8	-23.4	-21.0	-14.6	-7.2	-7.6	-4.5	-24.8	-6.0	-4.6	-6.0
	$\overline{D_f}$	-1.3	-3.3	-2.5	-4.8	-3.0	-1.7	-2.3	-1.8	-2.6	-1.0	-0.8	-0.9
	$D_f(max)$	-4.2	-13.2	-19.3	-12.0	-6.7	-4.0	-6.0	-4.3	-19.3	-4.1	-5.7	-5.7
	$\overline{DD}$	-2.6	-9.1	-5.9	-10.5	-6.7	-4.0	-4.4	-3.2	-5.8	-1.8	-1.2	-1.5
	$DD(max)$	-10.6	-36.8	-42.7	-33.0	-21.2	-11.1	-13.6	-8.0	-42.7	-10.1	-10.3	-10.3
	$\overline{D_f}/\overline{DD}$ (%)	50	36	42	46	45	43	52	56	45	56	67	60
DREff	$\overline{D_c}$	-53.3	-48.9	-56.7	-46.5	-38.6	-32.7	-28.2	-20.5	-43.9	-51.9	-46.3	-49.9
	$D_c(max)$	-101.9	-102.3	-99.4	-101.1	-96.3	-83.1	-82.9	-84.2	-102.3	-92.3	-70.4	-92.3
	$\overline{D_f}$	-97.7	-134.2	-119.6	-103.1	-86.3	-75.8	-78.8	-68.6	-98.6	-111.8	-122.3	-116.9
	$D_f(max)$	-173.6	-179.6	-181.0	-185.7	-182.8	-146.1	-145.6	-144.7	-185.7	164.1	-136.0	-164.1
	$\overline{DD}$	-67.7	-64.4	-72.8	-62.1	-51.2	-43.5	-43.5	-35.4	-58.0	-71.7	-75.8	-73.4
	$DD(max)$	-122.5	-121.3	-117.3	-121.9	-113.0	-94.0	-101.6	-103.2	-122.5	-113.4	-113.0	-113.4

(*) 29 and 30 June represent the first and second DD episode, respectively, as observed in LPZ.

4 Discussion

Dust forecast modelling and back-trajectory analysis show that the main part of the air masses arriving to BCN during the dusty period studied (23-30 June 2019) originated in the Saharan region. In the case of LPZ, air masses were coming mostly from the Iberian Peninsula, which was still under dusty conditions for the same period, and just a few were coming straight from the Sahara. However, the dust air masses pathways are different for the two consecutive dust episodes observed in LPZ: for the first one, dust air masses arrived from the Iberian Peninsula describing a left-side arch coming from the North, slightly crossing central Europe, meanwhile, for the second one, they arrived from the Iberian Peninsula, directly crossing Europe to LPZ. Indeed, differences found in the vertical optical and mass impact, and consequently in the DRE, of the dust particles are based on the singular dust transport to both distant BCN and LPZ stations.

Both AERONET data and MPLNET observations were used for continuous monitoring of the dust outbreak and the retrieval of the dust properties in order to calculate the DRE. By using the synergy between the POLIPHON method and polarized MPL measurements, the vertical profiles of the dust coarse (Dc) and dust fine (Df) extinction coefficient (and the mass concentration as well) were identified, and hence the Dc and Df contribution to the total dust (DD=Dc+Df) DRE was estimated.

At BCN mean dust optical depth values at 532 nm (DOD^{532}) for Dc, Df and DD particles, respectively, of 0.116, 0.037 and 0.153, with DD DOD^{532} peaks of 0.63 (AE ~ 0.19), were found. Also, moderately absorbing particles, SSA^{440}=0.94, and different asymmetry factors for Dc (asyF^{440} = 0.86) and Df and (asyF^{440} = 0.63) particles were also reported in BCN. At LPZ the dust incidence was weaker as compared to BCN: the mean DOD^{532} for each of the two dust episodes for Dc, Df and DD particles in percentage with respect to DOD^{532} in BCN was, respectively, 24%, 43% and 29% for the first dust episode, and 17%, 35% and 22% for the second one. Similar moderately absorbing particles (SSA^{440}=0.94-0.95), and asyF^{440} values for Dc and Df of 0.86 and 0.61, respectively, were reported for the two dust episodes in LPZ as well. Mean Df/DD DOD^{532} ratios of

24% and 36% (39%) were found, respectively, in BCN for the whole dust event and LPZ for the first (second) dust episode; hence, the Df contribution is higher in LPZ with respect to BCN. Indeed, this result reflects the aging of dust, and in particular the gravitational settling of Dc particles during their longer transport to LPZ.

Regarding the vertical extent and structure of dust particles, the dust intrusion was gradually moving on along the whole dust event (23-30 June) in BCN, reaching altitudes mainly from 1 to 5-6 km height with presence of both Dc and Df particles; PLDR values of 0.2-0.3 also pointed out the predominance of Dc particles. In the case of LPZ, a two-layered structure with a well-defined decoupled dust layer between 3 and 5.5 km height with PLDR of 0.35-0.39 (practically only Dc presence) is observed for the first episode, while a mixture of Dc, Df and ND particles is clearly observed during the second event. These differences are related to the singular intrusion pathway of each dust episode; during the second episode, unlike what happened during the first one, air masses were coming from the Iberian Peninsula, directly crossing central Europe, and thus allowing a high degree of dust mixing. Concerning the relative mass incidence of each component, Dc particles were dominating (around 80%, in general) along the overall dusty period in both stations. However, a higher Df mass contribution with respect to the total dust mass loading was found in LPZ (13.5%) than in BCN (11%), reflecting again, through an increase of the fine mode mass contribution, the aging of the dust. The mean daily-averaged total mass loading was higher in BCN (0.31±0.19 g m^{-2}) than in LPZ (36% of that found in BCN). As also stated before, this is a consequence of the particular transport of the dust intrusions to BCN and LPZ, which is also reflected, according to the daily-averaged CoM height, in the vertical impact of the dust intrusions over each station. In BCN, the evolution of the CoM height follows a similar descending pattern from around 3 km on 24 June down to 2 km height on 30 June, but the mean CoM height for Df particles is slightly higher than that for the Dc component (200-250 m difference) since 27 June until the end of the dust event. These results might indicate loss of the large particles during the progression of the dust intrusion over BCN. The mean CoM height of the dust particles is greater in LPZ (between 3 and 4 km) than in BCN (at 2-3 km height). Since the dust intrusion in LPZ, including both differentiated episodes, lasted only two days, the descending behaviour observed in BCN is not present.

In the context of the particular dust scenarios of BCN (continuous and progressive dust particles coming from the Sahara region) and LPZ (two close but separated dust episodes: the first introducing a well-defined high decoupled dust layer with mostly Dc presence, and the second presenting a high degree of dust mixing), the DRE (and DREff) at the surface (SRF) and at the TOA, and also the atmospheric DRE (and its efficiency), were calculated for both stations. The modification of the dust optical properties due to aging and its impact on the DRE is evidenced with the temporal dust evolution in BCN and with the comparison between BCN and LPZ dust scenarios.

On one hand, in BCN, themean daily DRE on the surface, $DRE(SRF)$, for the total dust (DD=Dc+Df) was -9 ± 4 W·m^{-2}, with an instantaneous maximum of -54.5 W·m^{-2} while the total dust mean daily $DREff(SRF)$ was -89 ± 4 W·m^{-2} τ^{-1},with an instantaneous peak of -133.7 W·m^{-2} τ^{-1}. The daily Df/DD DRE ratio at the surface was 37%, being > 24% for Df/DD DOD ratio; that is, in relative terms, Df particles contribute more to the total dust DRE than they did to the DOD. This was also observed in the DREff on the surface: $DREff(SRF)$ is higher in absolute value for Df particles (-130 ± 1 W·m^{-2} τ^{-1}) than for Dc ones (-75 ± 3 W·m^{-2} τ^{-1}). The driving factor of that is the asymmetry factor: a lower asyF value is found for the fine mode (0.63) than for the coarse one (0.86). As a consequence and compared with a pure forward-scattering particle, there is more solar irradiance scattered in the atmosphere and thus less irradiance is arriving to the surface. In these conditions, it must be highlighted that, at constant AOD, the DRE at the surface for Df particles would be higher, in absolute values, than for Dc ones. Along the dust 8-day event in BCN, the effect of dust aging is clearly visible on the Df/DD DRE ratio at the surface, which increased at a rate of +2.4%·day^{-1}, i.e., +16% between the first and the last day of the event. That is, at the end of the dust period, the Df contribution to the total dust DRE at the surface was 44%, i.e., almost the same as for the Dc particles.

On the other hand, the total dust mean daily DRE at TOA (and the atmospheric DRE) was -6 ± 3 W·m^{-2} (+3 ± 7 W·m^{-2}) (instantaneous DRE peak at TOA of -42.7 W·m^{-2}). Regarding the DREff, a total dust mean daily value at TOA and the atmospheric one of -58 ± 6 W·m^{-2} τ^{-1} and +31 ± 10 W·m^{-2} τ^{-1}, respectively, were estimated, with an instantaneous DREff peak

at TOA of -122.5 $W \cdot m^{-2}$ τ^{-1}. The daily Df/DD DRE ratio at TOA was 45%, which is higher than the one found at the surface (37%). Hence, the contribution of the Df particles is stronger at the TOA than at the surface. Along the 8-day dust event, the Df/DD DRE ratio at TOA increased at a rate of $+2.9\% \cdot day^{-1}$, i.e. +20% between the first and the last day of the event. Then, at the end of the event the Df/DD DRE ratio at TOA was 56%, that is, the Df contribution to the total dust DRE is higher than the one found for the Dc particles. The atmospheric Df/DD DRE ratio was very similar to that estimated for DOD; additionally, the atmospheric DRE was found to be independent of the considered dust mode.

The results at LPZ are a kind of extension of what is observed in BCN, because the main origin of the dust intrusion is from the Iberian Peninsula, which was already under the Saharan dusty conditions that arrived at LPZ on 29 June. Hence, dust particles were travelling for a longer period to LPZ, likely experiencing a more pronounced gravitational settling of the largest particles. Although the total dust radiative cooling impact was much lower in LPZ (i.e., the mean total dust DRE was the 27.5% and 26%, respectively, on the surface and at the TOA, of that in BCN), the relevance of the DRE in LPZ relies on a two-fold aspect. Firstly, both consecutive dust episodes were caused by different dust air masses pathways coming from the Iberian Peninsula, as described before. Despite their similar columnar SSA pattern, a completely decoupled high dust layer was observed for the first one, and a more mixed dusty environment for the second one, , which suggested a certain dust-pollution mixing in both episodes. Indeed, this is an example of the advantage of using lidar measurements in characterizing aerosol complex scenarios: both DD and ND components were present in both episodes, but they were only 'mixed' in the second one. Second, and as a direct consequence of the dust aging, the mean Df/DD DRE ratio at the surface in LPZ was 52%, which is higher than in BCN (37%), likewise that observed at the TOA, where the Df/DD DRE ratio was 60% in LPZ and 45% in BCN. This might confirm, as mentioned before, the gravitational settling of the largest dust particles during a longer transport, leading to a higher contribution of Df particles to the total dust DRE in comparison with BCN. Moreover, the total dust DREff on the surface was -113 ± 1 W m^{-2} τ^{-1} in LPZ, which is a higher absolute value with respect to that found in BCN (-89 ± 4 W m^{-2} τ^{-1}). That apparent increase, in absolute value, is because of the spectral behaviour of the asyF, which was slightly smaller in LPZ than in BCN, and then, at constant AOD, a larger cooling effect (i.e., a larger radiative efficiency) was produced.

5 Summary and main conclusions

Aerosol radiative effects during the summer 2019 heatwave over Europe produced partly by an inter-continental Saharan dust outbreak have been assessed in this work. The continuous evolution of the dust direct radiative effect (DRE) in the SW range has been examined, in particular, for a case study of the dust intrusion observed in June 2019 at two European stations. The dust plume was firstly observed in Barcelona (BCN, Spain; 41.4ºN, 2.1ºE, 125 m a.s.l.) on 23 June, long-lasting for 8 days until 30 June (23-30 June). Later, it arrived at Leipzig (LPZ, Germany; 51.4ºN, 12.4ºE, 125 m a.s.l.) on 29 June, being detected two slightly separated different dust episodes for two consecutive days (29-30 June).

Main conclusions are summarized next:

- The particular pathway of the dust air masses defines the aerosol scenario, determining clearly the vertical extent and the properties of the dust particles, and hence, their direct radiative effects (DRE).
- Only columnar data do not fully describe that scenario and they can even lead to wrong dust characterization, but in synergy with lidar observations the dust environment can be completely analysed and assessed.
- The synergetic use of POLIPHON method with continuous P-MPL measurements allows the separation of the optical properties of both the Dc and Df components from the ND aerosols in a 24/7 temporal basis in order to evaluate separately the radiative effect of dust in mixed scenarios.
- A dust-induced cooling effect is observed in the SW range, being the DRE efficiency higher, in absolute value, at the surface than at the top-of-atmosphere (TOA).

- Despite Dc particles usually dominate under dusty conditions, the contribution of Df particles to the total dust DRE, both at the surface and at the TOA, is relevant; it is higher at the TOA than at the surface and in both cases it increases throughout the event; at the TOA, the Df contribution at the end of the event is even higher than Dc particles one (56 vs. 44 %).
- Consequently, although the dust cooling effect is lower in LPZ than in BCN, the Df contribution to the total dust DRE is higher in LPZ than in BCN because of the progressive loss of large particles by gravitational settling during their longer transport to the LPZ station.

The study calls for a more generalized use of state-of-the-art algorithms, like POLIPHON, to independently retrieve aerosol properties for the fine and coarse modes. These retrievals are very valuable when used as input of radiative transfer models. Our findings clearly demonstrate that both fine and coarse modes are equally relevant for the estimation of SW direct radiative effects of long-range transported mineral dust. In general, results obtained in this work are especially relevant for the next ESA EarthCARE mission (launch planned in 2022), which is focused on radiation-aerosol-cloud interactions, but also for satellite remote sensing instrumentation, which is mostly sensitive to SW wavelengths, since its measurements can be likely affected by dust contamination. In addition, the determination of the dust ice nucleating particle (INP) concentration, once separated dust and non-dust components, is on-going; this is in relation with the indirect dust radiative forcing, representing an added-value in aerosol-cloud-radiation research. The dust longwave (LW) and net direct radiative effect of both Dc and Df modes on the surface and at TOA are presented in the companion paper by Sicard et al. (2021).

Data availability. Part of the data used in this publication were obtained as part of the AERONET and MPLNET networks and are publicly available. For additional data or information, please contact the authors.

Author Contributions. CC-J and MS designed the study and wrote the original draft paper. CC-J, MS and AA provided data. CC-J, MS and M-AL-C performed data analysis with contributions from AA, AC, M-PZ, AR-G- and CM-P. All authors reviewed and edited the final version of the manuscript. All the authors agreed to the final version of the paper.

Competing interests. The authors declare that they have no conflict of interest.

Acknowledgments. Authors thank the images provided from the NMMB/BSC-Dust model, operated by the Barcelona Supercomputing Centre (BSC) (https://ess.bsc.es/bsc-dust-daily-forecast). Authors also gratefully acknowledge the NOAA Air Resources Laboratory (ARL) for the provision of the pictures from the HYSPLIT transport and dispersion model and/or READY website (http://www.ready.noaa.gov) used in this work. The MPLNET project is funded by the NASA Radiation Sciences Program and Earth Observing System. Although none of the data of the paper have been extracted from MPLNET, the MPLNET staff at NASA GSFC is warmly acknowledged for the continuous help in keeping the MPL systems and the data analysis up-to-date. We particularly thank Judd Welton for providing the MPL unit in place at the Barcelona site.

Financial support. This research was funded by the Spanish Ministry of Science, Innovation and Universities (CGL2017-90884-REDT, PRX18/00137-Programa "Salvador de Madariaga"), the Spanish Ministry of Science and Innovation (PID2019-104205GB-C21, PID2019-103886RB-I00), the H2020 program from the European Union (GA no. 654109, 778349, 871115), and the Unity of Excellence “María de Maeztu“ (MDM-2016-0600) financed by the Spanish State Research Agency (AEI). M-PZ has been partially funded by the AEI (MDM-2017-0737, Unity of Excellence “María de Maeztu” - Centro de Astrobiología (CSIC-INTA)). M-AL-C is supported by the INTA predoctoral contract programme.

References

Akritidis, D., Katragkou, E., Georgoulias, A. K., Zanis, P., Kartsios, S., Flemming, J., Inness, A., Douros, J., and Eskes, H.: A complex aerosol transport event over Europe during the 2017 Storm Ophelia in CAMS forecast systems: analysis and evaluation, Atmos. Chem. Phys., 20, 13557–13578, https://doi.org/10.5194/acp-20-13557-2020, 2020.

Ansmann, A., Bösenberg, J., Chaikovsky, A., Comerón, A., Eckhardt, S., Eixmann, R., Freudenthaler, V., Ginoux, P., Komguem, L., Linné, H., Márquez, M. Á. L., Matthias, V., Mattis, I., Mitev, V., Müller, D., Music, S., Nickovic, S., Pelon, J., Sauvage, L., Sobolewsky, P., Srivastava, M. K., Stohl, A., Torres, O., Vaughan, G., Wandinger, U., and Wiegner, M.: Long-range transport of Saharan dust to northern Europe: The 11–16 October 2001 outbreak observed with EARLINET, J. Geophys. Res.-Atmos., 108, 4783, https://doi.org/10.1029/2003JD003757, 2003.

Ansmann, A.; Rittmeister, F.; Engelmann, R.; Basart, S.; Jorba, O.; Spyrou, C.; Remy, S.; Skupin, A.; Baars, H.; Seifert, P. : Profiling of Saharan Dust from the Caribbean to Western Africa-Part 2: Shipborne Lidar Measurements Versus Forecasts, Atmos. Chem. Phys., 17, 14987-15006, https://doi.org/10.5194/acp-17-14987-2017, 2017.

Ansmann, A.; Mamouri, R.; Hofer, J.; Baars, H.; Althausen, D.; Abdullaev, S.F.: Dust Mass, Cloud Condensation Nuclei, and Ice-Nucleating Particle Profiling with Polarization Lidar: Updated POLIPHON Conversion Factors from Global AERONET Analysis, Atmos. Meas. Tech., 12, 4849-4865, https://doi.org/10.5194/amt-12-4849-2019, 2019.

Balkanski, Y., Schulz, M., Claquin, T., and Guibert, S.: Reevaluation of Mineral aerosol radiative forcings suggests a better agreement with satellite and AERONET data, Atmos. Chem. Phys., 7, 81–95, https://doi.org/10.5194/acp-7-81-2007, 2007.

Banks, J.R.; Brindley, H.E.; Hobby, M.; Marsham, J.H.: The Daytime Cycle in Dust Aerosol Direct Radiative Effects Observed in the Central Sahara during the Fennec Campaign in June 2011, J. Geophys. Res. Atmos., 119, 13,861-13,876, https://doi.org/10.1002/2014JD022077, 2014

Cachorro, V.E.; Toledano, C.; Prats, N.; Sorribas, M.; Mogo, S.; Berjón, A.; Torres, B.; Rodrigo, R.; De la Rosa, J.; De Frutos, A.M.: The Strongest Desert Dust Intrusion Mixed with Smoke Over the Iberian Peninsula Registered with Sun Photometry, J. Geophys. Res. Atmos., 113, D14S04. https://doi.org/10.1029/2007JD009582, 2008.

Campbell, J.R.; Hlavka, D.L.; Welton, E.J.; Flynn, C.J.; Turner, D.D.; Spinhirne, J.D.; Scott III, V.S.; Hwang, I.H.: Full-Time, Eye-Safe Cloud and Aerosol Lidar Observation at Atmospheric Radiation Measurement Program Sites: Instruments and Data Processing, J. Atmos. Ocean. Technol., 19, 431-442, https://doi.org/10.1175/1520-0426(2002)019<0431:FTESCA>2.0.CO;2, 2002.

Córdoba-Jabonero, C., Sorribas, M., Guerrero-Rascado, J.L., Adame, J.A., Hernández, Y., Lyamani, H., Cachorro, V., Gil, M., Alados-Arboledas, L., Cuevas, E., De la Morena, B.: Synergetic monitoring of Saharan dust plumes and potential impact on surface: a case study of dust transport from Canary Islands to Iberian Peninsula, Atmos. Chem. Phys. 11, 3067e3091. http://dx.doi.org/10.5194/acp-11-3067-2011, 2011.

Córdoba-Jabonero, C.; Andrey-Andres, J.; Gomez, L.; Adame, J.A.; Sorribas, M.; Navarro-Comas, M.; Puentedura, O.; Cuevas, E.; Gil-Ojeda, M.: Vertical Mass Impact and Features of Saharan Dust Intrusions Derived from Ground-Based Remote Sensing in Synergy with Airborne in-Situ Measurements, Atmos. Environ., 142, 420-429, https://doi.org/10.1016/j.atmosenv.2016.08.003, 2016.

Córdoba Jabonero, C.; Sicard, M.; Ansmann, A.; del Águila, A.; Baars, H.: Separation of the Optical and Mass Features of Particle Components in Different Aerosol Mixtures by using POLIPHON Retrievals in Synergy with Continuous Polarized Micro-Pulse Lidar (P-MPL) Measurements, Atmos. Meas. Tech., 11, 4775-4795, https://doi.org/10.5194/amt-11-4775-2018, 2018.

Córdoba-Jabonero, C.; Sicard, M.; Del Águila, A.; Jiménez, M.; Zorzano, M.: Performance of a Dust Model to Predict the Vertical Mass Concentration of an Extreme Saharan Dust Event in the Iberian Peninsula: Comparison with Continuous, Elastic, Polarization-Sensitive Lidars, Atmos. Environ., 214, 116828, https://doi.org/10.1016/j.atmosenv.2019.116828, 2019.

DeMott, P.J.; Sassen, K.; Poellot, M.R.; Baumgardner, D.; Rogers, D.C.; Brooks, S.D.; Prenni, A.J.; Kreidenweis, S.M.: African Dust Aerosols as Atmospheric Ice Nuclei, Geophys. Res. Lett., 30, 14, 1732, 2003.

Derimian, Y.; León, J.; Dubovik, O.; Chiapello, I.; Tanré, D.; Sinyuk, A.; Auriol, F.; Podvin, T.; Brogniez, G.; Holben, B.N.: Radiative Properties of Aerosol Mixture Observed during the Dry Season 2006 Over M'Bour, Senegal (African Monsoon Multidisciplinary Analysis Campaign), J. Geophys. Res. Atmos., 113, D00C09. https://doi.org/10.1029/2008JD009904, 2008.

Di Biagio, C.; di Sarra, A.; Meloni, D.; Monteleone, F.; Piacentino, S.; Sferlazzo, D.: Measurements of Mediterranean Aerosol Radiative Forcing and Influence of the Single Scattering Albedo, J. Geophys. Res. Atmos., 114, https://doi.org/10.1029/2008JD011037, 2009.

Di Sarra, A.; Pace, G.; Meloni, D.; De Silvestri, L.; Piacentino, S.; Monteleone, F.: Surface Shortwave Radiative Forcing of Different Aerosol Types in the Central Mediterranean, Geophys. Res. Lett., 35, 2, https://doi.org/10.1029/2007GL032395, 2008.

Draxler, R.R.; Hess, G.D.: An Overview of the HYSPLIT_4 Modelling System for Trajectories, Aust. Meteorol. Mag., 47, 295-308, 1998.

Dubovik, O., Smirnov, A., Holben, B. N., King, M. D., Kaufman, Y. J., Eck, T. F., and Slutsker, I.: Accuracy assessment of aerosol optical properties retrieval from AERONET sun and sky radiance measurements, J. Geophys. Res., 105, 9791–9806, https://doi.org/10.1029/2000JD900040, 2000.

Dubovik, O.; Holben, B.; Eck, T.F.; Smirnov, A.; Kaufman, Y.J.; King, M.D.; Tanré, D.; Slutsker, I.: Variability of Absorption and Optical Properties of Key Aerosol Types Observed in Worldwide Locations, J. Atmos. Sci., 59, 590-608, https://doi.org/10.1175/1520-0469(2002)059<0590:VOAAOP>2.0.CO;2, 2002.

Dubovik, O., Sinyuk, A., Lapyonok, T., Holben, B. N., Mishchenko, M., Yang, P., Eck, T. F., Volten, H., Muñoz, O., Veihelmann, B., van der Zande, W. J., Leon, J.-F., Sorokin, M., and Slutsker, I.: Application of spheroid models to account for aerosol particle nonsphericity in remote sensing of desert dust, J. Geophys. Res., 111, D11208, https://doi.org/10.1029/2005JD006619, 2006.

Dubuisson, P.; Buriez, J.C.; Fouquart, Y.: High Spectral Resolution Solar Radiative Transfer in Absorbing and Scattering Media: Application to the Satellite Simulation, J Quant. Spectrosc. Radiat. Transf., 55, 103-126, https://doi.org/10.1016/0022-4073(95)00134-4, 1996.

Dubuisson, P.; Dessailly, D.; Vesperini, M.; Frouin, R.: Water Vapor Retrieval Over Ocean using Near-infrared Radiometry, J. Geophys. Res. Atmos., 109. D19106. https://doi.org/10.1029/2004JD004516, 2004.

Dubuisson, P., Roger, J., Mallet, M., and Dubovik, O.: A Code to Compute the Direct Solar Radiative Forcing: Application to Anthropogenic Aerosols during the Escompte Experiment, Proc. International Radiation Symposium (IRS 2004) on Current Problems in Atmospheric Radiation, edited by: Fischer, H., Sohn, B.-J., and Deepak, A., Hampton, 127–130, 23–28 August 2004, Busan, Korea, 2006.

Eck, T. F., Holben, B. N., Reid, J. S., Dubovik, O., Kinne, S., Smirnov, A., O'Neill, N. T., and Slutsker, I.: Wavelength dependence of the optical depth of biomass burning, urban and desert dust aerosols, J. Geophys. Res., 104, 31333–31349, https://doi.org/10.1029/1999JD900923, 1999.

Fernald, F.G.: Analysis of Atmospheric Lidar Observations: Some Comments, Appl. Opt., 23, 652-653, 1984.

Flynn, C.J.; Mendozaa, A.; Zhengb, Y.; Mathurb, S.: Novel Polarization-Sensitive Micropulse Lidar Measurement Technique, Opt. Express, 15, 2785-2790, https://doi.org/10.1364/OE.15.002785, 2007.

Ginoux, P., Prospero, J. M., Gill, T. E., Hsu, N. C., Zhao, M.: Global-scale attribution of anthropogenic and natural dust sources and their emission rates based on MODIS Deep Blue aerosol products, Rev. Geophys., 50, RG3005, https://doi.org/10.1029/2012RG000388, 2012.

Granados-Muñoz, M.J.; Sicard, M.; Román, R.; Benavent-Oltra, J.A.; Barragán, R.; Brogniez, G.; Denjean, C.; Mallet, M.; Formenti, P.; Torres, B.: Impact of Mineral Dust on Shortwave and Longwave Radiation: Evaluation of Different Vertically

Resolved Parameterizations in 1-D Radiative Transfer Computations, Atmos. Chem. Phys., 19, 523–542. https://doi.org/10.5194/acp-19-523-2019, 2019.

Halthore, R.N.; Crisp, D.; Schwartz, S.E.; Anderson, G.P.; Berk, A.; Bonnel, B.; Boucher, O.; Chang, F.; Chou, M.; Clothiaux, E.E; Dubuisson, P.; Fomin, B.; Fouquart, Y.; Freidenreich, S.; Gautier, C.; Kato, S., Laszlo, I.; Li, Z.; Mather, J.H.; Plana-Fattori, A.; Ramaswamy, V.; Ricchiazzi, P.; Shiren, Y.; Trishchenko, A.; Wiscombe, W.: Intercomparison of Shortwave Radiative Transfer Codes and Measurements, J. Geophys. Res. Atmos., 110, D11206. https://doi.org/10.1029/2004JD005293, 2005.

Haywood, J., and O. Boucher: Estimates of the Direct and Indirect Radiative Forcing due to Tropospheric Aerosols: A Review, Reviews of Geophysics, 38, 513–543, 2000.

Hess, M., Koepke, P., Schult, I.: Optical properties of aerosols and clouds: the software package OPAC, Bull. Am. Meteorol. Soc. 79, 831–844. https://doi.org/10.1175/1520-0477(1998)079%3c0831:OPOAAC%3e2.0.CO;2, 1998.

Huneeus, N., Schulz, M.; Balkanski, Y., Griesfeller, J., Prospero, J., Kinne, S., Bauer, S., Boucher, O., Chin, M., Dentener, F., Diehl, T., Easter, R., Fillmore, D., Ghan, S., Ginoux, P., Grini, A., Horowitz, L., Koch, D., Krol, M. C., Landing, W., Liu, X., Mahowald, N., Miller, R., Morcrette, J.-J., Myhre, G., Penner, J., Perlwitz, J., Stier, P., Takemura, T., Zender, C. S.: Global dust model intercomparison in AeroCom phase I, Atmos. Chem. Phys., 11, 7781–7816, https://doi.org/10.5194/acp-11-7781-2011, 2011.

IPCC 2013. Myhre, G., Shindell, D., Pongratz, J.,: Anthropogenic and natural radiative forcing. In: Stocker, T.F., Qin, D., Plattner, G.K., Tignor, M., Allen, S.K., Boschung, J., Midgley, P.M. (Eds.), Climate Change 2013: The Physical Science Basis. Contribution of Working Group I to the Fifth Assessment Report of the Intergovernmental Panel on Climate Change. Cambridge University Press, Cambridge, NY, USA, 2013.

Janjic, Z.; Janjic, T.; Vasic, R.: A Class of Conservative Fourth-Order Advection Schemes and Impact of Enhanced Formal Accuracy on Extended-Range Forecasts, Mon. Weather Rev., 139, 1556-1568, https://doi.org/10.1175/2010MWR3448.1, 2011.

Klett, J.D.: Lidar Inversion with Variable Backscatter/Extinction Ratios, Appl. Opt., 24, 1638-1643, 1985.

Lacis, A.A.; Oinas, V.: A Description of the Correlated K Distribution Method for Modeling Nongray Gaseous Absorption, Thermal Emission, and Multiple Scattering in Vertically Inhomogeneous Atmospheres, J. Geophys. Res. Atmos., 96, 9027-9063, https://doi.org/10.1029/90JD01945, 1991.

Liao, H.; Seinfeld, J.H.: Radiative Forcing by Mineral Dust Aerosols: Sensitivity to Key Variables, J. Geophys. Res. Atmos., 103, 31637-31645, https://doi.org/10.1029/1998JD200036, 1998.

Lyamani, H.; Olmo, F.J.; Alcántara, A.; Alados-Arboledas, L.: Atmospheric Aerosols during the 2003 Heat Wave in Southeastern Spain II: Microphysical Columnar Properties and Radiative Forcing, Atmos. Environ., 40, 6465-6476, https://doi.org/10.1016/j.atmosenv.2006.04.047, 2006.

Mallet, M.; Pont, V.; Liousse, C.: Modelling of Strong Heterogeneities in Aerosol Single Scattering Albedos Over a Polluted Region, Geophys. Res. Lett., 32, L09807. https://doi.org/ 0.1029/2005GL022680, 2005.

Mallet, M.; Pont, V.; Liousse, C.; Gomes, L.; Pelon, J.; Osborne, S.; Haywood, J.; Roger, J.; Dubuisson, P.; Mariscal, A.: Aerosol Direct Radiative Forcing Over Djougou (Northern Benin) during the African Monsoon Multidisciplinary Analysis Dry Season Experiment (Special Observation Period-0), J. Geophys. Res. Atmos., 113, D00C01, https://doi.org/ 10.1029/2007JD009419, 2008.

Mamouri, R.; Ansmann, A.: Fine and Coarse Dust Separation with Polarization Lidar, Atmos. Meas. Tech., 7, 3717–3735, https://doi.org/10.5194/amt-7-3717-2014, 2014.

Mamouri, R.; Ansmann, A.: Potential of Polarization/Raman Lidar to Separate Fine Dust, Coarse Dust, Maritime, and Anthropogenic Aerosol Profiles, Atmos. Meas. Tech., 10, 3403–3427, https://doi.org/10.5194/amt-10-3403-2017, 2017.

Marquis, J. W., Oyola, M. I., Campbell, J. R., Ruston, B. C., Córdoba-Jabonero, C., Cuevas, E., Lewis, J., Toth, T., Zhang, J.: Conceptualizing the Impact of Dust Contaminated Infrared Radiances on Data Assimilation for Numerical Weather Prediction, J. Atmos. Ocean. Techn., 38(2), 209-221, https://doi.org/10.1175/JTECH-D-19-0125.1, 2021.

Meloni, D.; Di Sarra, A.; Di Iorio, T.; Fiocco, G.: Influence of the Vertical Profile of Saharan Dust on the Visible Direct Radiative Forcing, J Quant Spectrosc Radiat Transf., 93, 397-413, https://doi.org/10.1016/j.jqsrt.2004.08.035, 2005.

Meloni, D.; Junkermann, W.; Di Sarra, A.; Cacciani, M.; De Silvestri, L.; Di Iorio, T.; Estellés, V.; Gómez-Amo, J.L.; Pace, G.; Sferlazzo, D.M.: Altitude-resolved Shortwave and Longwave Radiative Effects of Desert Dust in the Mediterranean during the GAMARF Campaign: Indications of a Net Daily Cooling in the Dust Layer, J. Geophys. Res. Atmos., 120, 3386-3407, https://doi.org/10.1002/2014JD022312, 2015.

Mona, L., Amodeo, A., Pandolfi, M., and Pappalardo, G.: Saharan dust intrusions in the Mediterranean area: Three years of Raman lidar measurements, J. Geophys. Res.-Atmos., 111, D16203, https://doi.org/10.1029/2005JD006569, 2006.

Osborne, S.R.; Baran, A.J.; Johnson, B.T.; Haywood, J.M.; Hesse, E.; Newman, S.: Short-wave and Long-wave Radiative Properties of Saharan Dust Aerosol, Q. J. R. Meteorol. Soc., 137, 1149-1167, https://doi.org/10.1002/qj.771, 2011.

Osborne, M., Malavelle, F. F., Adam, M., Buxmann, J., Sugier, J., Marenco, F., and Haywood, J.: Saharan dust and biomass burning aerosols during ex-hurricane Ophelia: observations from the new UK lidar and sun-photometer network, Atmos. Chem. Phys., 19, 3557–3578, https://doi.org/10.5194/acp-19-3557-2019, 2019.

Osipov, S.; Stenchikov, G.L.; Brindley, H.; Banks, J.: Diurnal Cycle of the Dust Instantaneous Direct Radiative Forcing Over the Arabian Peninsula, Atmos. Chem. Phys. 2015, 15, 9537–9553. https://doi.org/10.5194/acp-15-9537-2015.

Papayannis, A., Balis, D., Amiridis, V., Chourdakis, G., Tsaknakis, G., Zerefos, C., Castanho, A. D. A., Nickovic, S., Kazadzis, S., and Grabowski, J.: Measurements of Saharan dust aerosols over the Eastern Mediterranean using elastic backscatter-Raman lidar, spectrophotometric and satellite observations in the frame of the EARLINET project, Atmos. Chem. Phys., 5, 2065–2079, https://doi.org/10.5194/acp-5-2065-2005, 2005.

Papayannis, A., Amiridis, V., Mona, L., Tsaknakis, G., Balis, D., Bösenberg, J., Chaikovski, A., De Tomasi, F., Grigorov, I., Mattis, I., Mitev, V., Müller, D., Nickovic, S., Pérez, C., Pietruczuk, A., Pisani, G., Ravetta, F., Rizi, V., Sicard, M., Trickl, T., Wiegner, M., Gerding, M., Mamouri, R. E., D'Amico, G., and Pappalardo, G.: Systematic lidar observations of Saharan dust over Europe in the frame of EARLINET (2000–2002), J. Geophys. Res.-Atmos., 113, D10204, https://doi.org/10.1029/2007JD009028, 2008.

Pérez, C., Nickovic, S., Pejanovic, G., Baldasano, J. M., and Özsoy, E.: Interactive dust-radiation modeling: A step to improve weather forecasts, J. Geophys. Res., 111, D16206, https://doi.org/10.1029/2005JD006717, 2006.

Pérez García-Pando, C.; Haustein, K.; Jorba Casellas, O.; Janjic, Z.; Huneeus, N.; Baldasano Recio, J.M.; Black, T.; Basart, S.; Nickovic, S.; Miller, R.L.: Atmospheric Dust Modeling from Meso to Global Scales with the Online NMMB/BSC-Dust model-Part 1: Model Description, Annual Simulations and Evaluation, Atmos. Chem. Phys., 11, 13001-13027, https://doi.org/10.5194/acp-11-13001-2011, 2011.

Prospero, J. M., Ginoux, P., Torres, O., Nicholson, S. E., and Grill, T. E.: Environmental characterization of global sources of atmospheric soil dust identified with the Nimbus 7 Total Ozone Mapping Spectrometer (TOMS) absorbing aerosol product, Rev. Geophys., 40, 1002, doi:10.1029/2000RG000095, 2002.

Roger, J.; Mallet, M.; Dubuisson, P.; Cachier, H.; Vermote, E.; Dubovik, O.; Despiau, S.: A Synergetic Approach for Estimating the Local Direct Aerosol Forcing: Application to an Urban Zone during the Expérience Sur Site Pour Contraindre Les Modèles De Pollution Et De Transport D'Emission (ESCOMPTE) Experiment, J. Geophys. Res. Atmos., 111, https://doi.org/10.1029/2005JD006361, 2006.

Rolph, G.; Stein, A.; Stunder, B.: Real-Time Environmental Applications and Display System: READY, Environ Model Softw., 95, 210-228, https://doi.org/10.1016/j.envsoft.2017.06.025, 2017.

Sicard, M.; Mallet, M.; García-Vizcaíno, D.; Comerón, A.; Rocadenbosch, F.; Dubuisson, P.; Muñoz-Porcar, C.: Intense Dust and Extremely Fresh Biomass Burning Outbreak in Barcelona, Spain: Characterization of their Optical Properties and Estimation of their Direct Radiative Forcing, Environ. Res. Lett., 7, 034016, https://doi.org/10.1088/1748-9326/7/3/034016, 2012.

Sicard, M.; Bertolín, S.; Mallet, M.; Dubuisson, P.; Comerón Tejero, A.: Estimation of Mineral Dust Long-Wave Radiative Forcing: Sensitivity Study to Particle Properties and Application to Real Cases in the Region of Barcelona, Atmos. Chem. Phys., 14, 9213-9231, https://doi.org/10.5194/acp-14-9213-2014, 2014a.

Sicard, M., Bertolín, S., Muñoz, C., Rodríguez, A., Rocadenbosch, F., and Comerõn, A.: Separation of aerosol fine- and coarse mode radiative properties: Effect on the mineral dust longwave, direct radiative forcing, Geophys. Res. Lett., 41, 6978–6985, https://doi.org/10.1002/2014GL060946, 2014b.

Sicard, M.; Barragán Cuesta, R.; Dulac, F.; Alados Arboledas, L.; Mallet, M.: Aerosol Optical, Microphysical and Radiative Properties at Regional Background Insular Sites in the Western Mediterranean, Atmos. Chem. Phys., 16, 12177-12203, htpps://doi.org/ 10.5194/acp-16-12177-2016, 2016.

Sicard, M., Córdoba-Jabonero, C., López-Cayuela, M.-A., Ansmann, A., Comerón, A., Zorzano, M.-P., Rodríguez-Gómez, A., and Muñoz-Porcar, C.: Aerosol radiative impact during the summer 2019 heatwave produced partly by an inter-continental Saharan dust outbreak. Part 2. Longwave and net dust direct radiative effect, Atmos. Chem. Phys., in preparation, 2021.

Sokolik, I. N. and Toon, O. B.: Direct radiative forcing by anthropogenic airborne mineral aerosols, Nature, 381, 681–683, https://doi.org/10.1038/381681a0, 1996.

Sousa, P.M., Barriopedro, D., Ramos, A.M., García-Herrera, R., Espírito-Santo, F., Trigo, R.M.: Saharan air intrusions as a relevant mechanism for Iberian heatwaves: The record breaking events of August 2018 and June 2019, Weather and Climate Extremes, 26, 100224, https://doi.org/10.1016/j.wace.2019.100224, 2019.

Stamnes, K.; Tsay, S.; Wiscombe, W.; Jayaweera, K.: Numerically Stable Algorithm for Discrete-Ordinate-Method Radiative Transfer in Multiple Scattering and Emitting Layered Media, Appl. Opt., 27, 2502-2509, https://doi.org/10.1364/AO.27.002502, 1988.

Stein, A.F.; Draxler, R.R.; Rolph, G.D.; Stunder, B.J.; Cohen, M.D.; Ngan, F.: NOAA's HYSPLIT Atmospheric Transport and Dispersion Modeling System, Bull. Am. Meteorol. Soc., 96, 2059-2077, https://doi.org/10.1175/BAMS-D-14-00110.1, 2015.

Toledano, C., Cachorro, V. E., Berjon, A., de Frutos, A. M., Sorribas, M., de la Morena, B. A., and Goloub, P.: Aerosol optical depth and Ångström exponent climatology at El Arenosillo AERONET site (Huelva, Spain), Q. J. Roy. Meteor. Soc., 133, 795–807, https://doi.org/10.1002/qj.54, 2007.

Tsikerdekis, A., Zanis, P., Georgoulias, A. K., Alexandri, G., Katragkou, E., Karacostas, T., and Solmon, F.: Direct and semi-direct radiative effect of North African dust in present and future regional climate simulations, Clim. Dynam., 53, 4311–4336, https://doi.org/10.1007/s00382-019-04788-z, 2019.

Zender, C. S., Miller, R. L., and Tegen, I.: Quantifying mineral dust mass budgets: Terminology, constraints, and current estimates, Eos Trans. Am. Geophys. Union, 85, 509-512, https://doi.org/10.1029/2004EO480002, 2004.